DEVELOPMENT OF MULTICOLOR QUANTUM WELL INFRARED PHOTODETECTORS FOR MID- AND LONG-WAVELENGTH DETECTION

By

JUNG-CHI CHIANG

DISSERTATION PRESENTED TO THE GRADUATE SCHOOL
OF THE UNIVERSITY OF FLORIDA IN PARTIAL FULFILLMENT
OF THE REQUIREMENTS FOR THE DEGREE OF
DOCTOR OF PHILOSOPHY

UNIVERSITY OF FLORIDA

1997

ACKNOWLEDGMENTS

I wish to express my deep gratitude to the chairman of my supervisory committee, Dr. Sheng S. Li, for all his guidance, patience, and encouragement throughout the entire research process. I would like to extend my thanks to Dr. Gijs Bosman, Dr. Arnost Neugroschel, Dr. Robert M. Park, and Dr. Meimei Z. Tidrow for serving on my supervisory committee.

I would like to thank Drs. Ping-Chang Yang, Yanhua Wang, and Yeong-Chen Wang for their great help in semiconductor processing and design. Thanks are extended to my laboratory colleagues, Drs. Yun-Shan Chang and Daniel C. Wang, Jerome Chu, Dr. Ming-Yeh Chuang, Jung Hee Lee, and Chia-Hua Huang for their friendship and valuable assistant in the device fabrication and measurements.

I am greatly indebted to my wife, sons, mother, and parents-in-law for their unconditional love, patience, and support during the course of this study.

Finally, the financial support of ARPA and US Air Force Material Command is gratefully acknowledged.

TABLE OF CONTENTS

Page

ACKNOWLEDGMENTS ii

ABSTRACT v

1 INTRODUCTION 1

2 THEORETICAL CONSIDERATIONS 8

2.1 Introduction 8
2.2 Electronic States in Quantum Well 8
2.3 Strain Effects on the Energy Bandgap 12
2.4 Intersubband Transition 13
2.5 Performance of the Quantum Well Infrared Photodetectors 15

3 A GAAS/ALAS/ALGAAS AND GAAS/ALGAAS STACKED QUANTUM WELL INFRARED PHOTODETECTOR FOR 3 – 5 AND 8 – 14 μm DETECTION 21

3.1 Introduction 21
3.2 Device Growth and Fabrication 21
3.3 Results and Discussion 23
3.4 Conclusions 25

4 A VOLTAGE-TUNABLE MULTICOLOR TRIPLE-COUPLED INGAAS/GAAS/ALGAAS QUANTUM WELL INFRARED PHOTODETECTOR FOR 7 – 14 μm DETECTION 32

4.1 Introduction 32
4.2 Device Growth and Fabrication 33
4.3 Results and Discussion 33
4.4 Conclusions 37

5 A TWO-STACK TWO-COLOR HIGH STRAIN QUANTUM WELL INFRARED PHOTODETECTOR.....44

5.1 Introduction.....44
5.2 Device Growth and Fabrication.....45
5.3 Results and Discussion.....46
5.4 Conclusions.....48

6 A TWO-STACK INDIRECT-BARRIER/TRIPLE-COUPLED QUANTUM WELL INFRARED PHOTODETECTOR.....57

6.1 Introduction.....57
6.2 Device Growth and Fabrications.....58
6.3 Results and Discussion.....59
    6.3.1 LWIR TC-QWIPs.....60
        6.3.1.1 Effects of doping density.....60
        6.3.1.2 Effects of the QW periods.....61
    6.3.2 MWIR IB-QWIPs.....61
    6.3.3 Stacked IB/TC-QWIPs.....62
        6.3.3.1 20-period Stacked IB/TC-QWIPs.....62
        6.3.3.2 40-period Stacked IB/TC-QWIPs.....63
6.4 Conclusions.....64

7 A HIGH PERFORMANCE HIGH STRAIN TRIPLE-COUPLED QUANTUM WELL INFRARED DETECTOR.....82

7.1 Introduction.....82
7.2 Device Growth and Fabrications.....83
7.3 Results and Discussion.....84
    7.3.1 Dark Current Measurements.....84
    7.3.2 Photoresponse Measurements.....84
    7.3.3 Detectivity.....86
7.4 Conclusions.....86

8 SUMMARY AND CONCLUSIONS.....98

APPENDICE

1 GLOSSARY OF SYMBOLS.....104
2 ACRONYMS.....108

REFERENCES.....110

BIOGRAPHICAL SKETCH.....115

Abstract of Dissertation Presented to the Graduate School
of the University of Florida in Partial Fulfillment of the
Requirements for the Degree of Doctor of Philosophy

DEVELOPMENT OF MULTICOLOR QUANTUM WELL INFRARED PHOTODETECTORS FOR MID- AND LONG-WAVELENGTH DETECTION

By

Jung-Chi Chiang

December 1997

Chairman: Sheng S. Li
Major Department: Electrical and Computer Engineering

In this work, three types of dual-band *n*-type quantum well infrared photodetectors (QWIPs) have been developed for 3 – 5 μm mid-wavelength infrared (MWIR) and 8 – 14 μm long-wavelength infrared (LWIR) detection. In addition, three different voltage-tunable multicolor triple-coupled (TC) QWIPs using lightly strain InGaAs/GaAs/AlGaAs and high-strain InGaAs/AlGaAs/InGaAs material systems have been developed for the LWIR detection.

We demonstrated a new voltage-tunable multicolor triple-coupled quantum well infrared photodetector (TC-QWIP) for LWIR detection. Using quantum confined Stark shift effect, the wavelengths tunability of two QWIPs by changing applied bias voltage is demonstrated in the wavelength range of 8.2 – 9.1 μm and 10.8 – 11.5 μm.

A high-strain two-stack, two-color QWIP has been demonstrated with high performance. The device has 35 % of indium in the QW of the MWIR stack which produces high in-plane compressive strain. The detection peak wavelengths are at 4.3 μm and 9.6 μm and the corresponding maximum responsivities are 0.65 A/W and 0.55 A/W for the MWIR and LWIR stacks, respectively, with 45° light incidence. Normal incidence without grating coupling also achieved responsivity of 0.25 A/W for either stack.

Characterizations of a two-stack indirect-barrier/triple-coupled (IB/TC)-QWIP, with two different doping densities ($N_d = 5\times10^{17}$ cm^{-3} and 1×10^{18} cm^{-3}) and different quantum well (QW) periods (20 and 40 periods), have been performed to study their effects on the performance of these devices. The responsivity of the MWIR IB-QWIPs was found to increase with increasing doping density, while for LWIR TC-QWIPs the responsivity was found to be independent of the doping density. Study of the effect of the QW periods revealed that the responsivity of the 20-period stacked-QWIPs is better than those of the 40-period stacked-QWIPs. The two-stack IB/TC-QWIPs reported here maybe used to detect simultaneously two colors in the MWIR and LWIR bands at the same bias voltage. It can also be used as a voltage tunable (PV and PC mode operation) two- or three-color QWIP for MWIR and LWIR dual band detection.

Finally, we demonstrated a very high performance TC-QWIP using high-strain (HS-) *n*-type $In_{0.25}Ga_{0.75}As/Al_{0.11}Ga_{0.89}As/In_{0.12}Ga_{0.88}As$ asymmetrical triple-coupled quantum well structure for 8 – 14 μm LWIR detection. The maximum detectivities at λ_p = 9.8 μm were found to be 1.44×10^{10} cm-Hz$^{1/2}$/W and 2.93×10^{10} cm-Hz$^{1/2}$/W, at V_b = -2.6 V and -4.5 V and T = 77 K for the 5- and 10-period devices, respectively. It is shown that this HS TC-QWIP can be used as a voltage-tunable two-color or multicolor QWIP for lower background LWIR detection.

CHAPTER 1
INTRODUCTION

Visible photons emitted by sun provide the most important source of radiation on earth, while the infrared (IR) radiation is the second most intensive radiation source. Infrared photodetectors have been extensively investigated in the past century [1]. In general, the infrared detectors can be classified as photon detectors and thermal detectors. In the first category, photons interact directly with the charge carriers in a material to generate a photocurrent. In the second category, it is characterized by the changes in certain properties of a material due to a change in temperature arising from absorption of the infrared radiation.

An infrared detector can be operating either in photovoltaic (PV) or photoconductive (PC) mode. In the PV mode detection, the device can be operated under zero bias condition while in PC mode detection a bias voltage has to be applied to the detector in order to get a photosignal. Most of the quantum well infrared photodetectors (QWIPs) are operating in PC mode detection, while HgCdTe (MCT) IR detectors are operating in PV mode detection.

The advent of epitaxial layer growth techniques such as Molecular Beam Epitaxy (MBE) [2] and Metalorganic Chemical Vapor Deposition (MOCVD) has made it possible to grow a wide variety of novel semiconductor heterostructures. Significant progress has been made in quantum wells and superlattice optoelectronic devices using these growth techniques. The quantum well is formed by using a thin layer (less than de Broglie wavelength) of narrow bandgap semiconductor sandwiched between the thin wider bandgap semiconductor barrier layers. The motion of the carriers perpendicular to the layers becomes quantized so that localized two-dimensional (2-D) subbands of quantized states are formed inside the quantum well [3].

The early proposals of using optical intersubband transitions in quantum wells for infrared detection were made by Chang et al. [4], Esaki and Sakaki [5], and Coon and Karunasiri [6]. The first experimental observations of the intersubband absorption in GaAs quantum wells were made by West and Eglash [7] and then by Harwit and Harris [8]. The first GaAs quantum well infrared photodetector (QWIP) demonstration was made by Levine et al. [9] in 1987. Since then, QWIPs based on bound-to-bound (BTB), bound-to-continuum (BTC) [10], and bound-to-miniband (BTM) [11] transitions have been widely investigated for the 3 – 5 μm mid-wavelength infrared (MWIR) and 8 – 14 μm long-wavelength infrared (LWIR) detection in the past ten years [12].

Recently, there is a considerable interest in the development of voltage-tunable multicolor QWIPs [13-20]. Figure 1.1 shows the schematic energy band diagrams of *n*-type QWIPs. Figure 1.2 shows the schematic energy band diagrams of *p*-type QWIPs and Fig. 1.3 shows those of *n*-type multicolor QWIPs. Due to the evolving requirements of future space surveillance systems, focal plane array (FPA) configurations and specifications are changing. The 3 – 5 μm MWIR spectral region is of particular interest as the cool targets such as reentry vehicles with greybody signatures that peak in this wavelength band. A dual-color FPA in the 3 –5 μm MWIR and 8 -14 μm LWIR bands with colocated pixels simplifies the infrared electro-optical sensor design and fabrication. Optical devices to split the beam and carefully alignment of the two-color FPAs are not required, and the signal processing is also simplified. Detectors sensitive in the aforementioned spectral bands are of particular interest to researchers who are developing ultra-low loss communication systems, remote and land based astronomical telescopes, seeking and tracking systems, spaceborne surveillance radars, medical diagnosis and evaluations, and environmental mapping and detection. Development of an infrared photodetector FPA for staring image sensor applications in both MWIR and LWIR spectral bands on the same chip is a very important step in meeting the needs and technological challenges of future infrared imaging applications; which include the forward looking infrared (FLIR) systems, space exploration and sensing systems, medical imaging, and basic scientific research [11]. Currently available Schottky barrier PtSi staring FPAs are being used in the 3 – 5 μm MWIR imaging applications, while the 8 – 14 μm LWIR band utilizes HgCdTe (MCT) hybrid staring FPAs. Because of MCT's volatility, high dislocation density, small wafer size, the large difference in the thermal expansion coefficients between the MCT FPA and the Si based readout circuits, and difficulties in the processing of MCT, progress has been slow in the development of high uniform, large area, and low cost MCT FPAs for LWIR applications. Therefore, the main motivation in this research is to develop a highly sensitive multicolor III-V QWIP for FPAs and other IR image sensor applications.

In chapter 2, we describe the fundamental device physics of the quantum well infrared photodetectors: (1) calculations of the electronic states in quantum well using the transfer matrix method (TMM), (2) calculations of the energy bandgap for a strained-layer, (3) description of the basic theory of the intersubband transition, and (4) discussing how to evaluate the performance of QWIPs.

Chapter 3 presents a new two-color stacked GaAs/AlAs/AlGaAs and GaAs/AlGaAs QWIP with PV and PC dual-mode operation for the 3 – 5 μm MWIR and 8 – 14 μm LWIR detection. The PV responsivity of the MWIR-QWIP was found to be 68 % of the PC responsivity, demonstrating the ability for an efficient PV mode operation at 3 – 5 μm MWIR band.

A new voltage-tunable multicolor triple-coupled (TC-) QWIP is depicted in chapter 4. Using quantum confined Stark shift effect, the wavelength tunability by the applied bias voltage in the wavelength range of 8.2 – 9.1 μm and 10.8 – 11.5 μm are demonstrated for QWIP- A and B, respectively.

Chapter 5 describes a high-strain two-stack InGaAs/GaAs/AlGaAs MWIR and GaAs/AlGaAs LWIR QWIP. The device use a 35 % of indium in the quantum well of the MWIR stack which produces a high in-plane compressive strain and also enhances the responsivity of the MWIR stack. Normal incidence without grating coupling also achieved with a responsivity of 0.25 A/W for either stack.

In chapter 6, we investigate the performance dependence of a two-stack indirect-barrier/triple-coupled (IB/TC-) QWIP on doping density and the QW period.

In chapter 7, we demonstrate a very high performance TC-QWIP for LWIR detection using high-strain (HS) $In_{0.25}Ga_{0.75}As/Al_{0.12}Ga_{0.88}As/In_{0.11}Ga_{0.89}As$ material systems. This HS TC-QWIP shows very large normal incidence absorption without using grating coupler.

Finally, chapter 8 gives the summary, conclusions, and recommendations for future research.

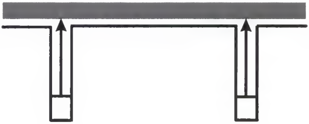

(a) BTC N-QWIP (Levine et al. [9])

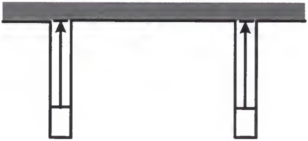

(b) BTQB N-QWIP (Gunapala et al. [60])

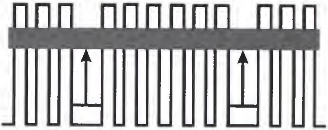

(c) BTM N-QWIP (Yu et al. [71])

Figure 1.1. Schematic energy band diagram of *n*-type QWIPs.

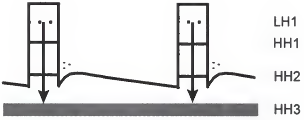

(a) TSL P-QWIP (Wang et al. [33])

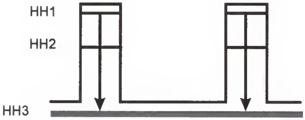

(b) CSL P-QWIP (Wang et al. [34])

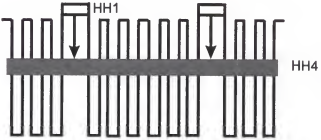

(c) SBTM P-QWIP (Chu et al. [35])

Figure 1.2. Schematic energy band diagrams of *p*-type QWIPs.

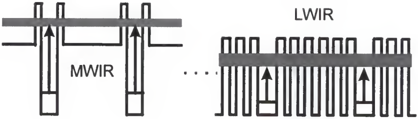

(a) 2-Stack 2-Color DB/BTM QWIP (Chap. 3)

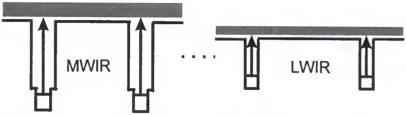

(b) 2-Stack 2-Color High Strain QWIP (Tidrow et al. [20] and Chap. 5)

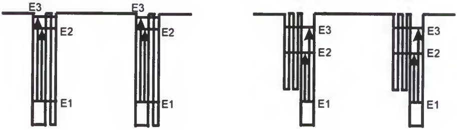

(c) Two-Coupled QWIP
(Tidrow et al. [62])

(d) Triple-Coupled QWIP
(Chap. 4)

Figure 1.3. Schematic energy band diagrams of *n*-type multicolor QWIPs.

CHAPTER 2
THEORETICAL CONSIDERATIONS

2.1 Introduction

Recent advances in epitaxial layer growth techniques such as MBE and MOCVD enable to grow the semiconductor monolayers with abrupt and atomically sharp interfaces. QWIPs made of III-V material systems offer several advantages over HgCdTe (MCT) detectors on the following reasons: (1) technologically mature device fabrication and materials processing techniques; (2) ease of crystal growth and lower cost; (3) a higher degree of uniformity which is of importance for FPAs; (4) radiation hardness; (5) tunability of upper cutoff wavelengths; and (6) compatible specific detectivity to that of HgCdTe.

Since the first observation of the intersubband transitions in a GaAs quantum well [7], rapid progress has been made in the development of high performance quantum well infrared photodetectors (QWIPs) [12]. Theoretical models [3, 21] have been developed to understand the performance limitation [22] and to achieve the device optimization [23] of QWIPs for specific applications. In this chapter we describe the fundamental device physics of QWIPs.

2.2 Electronic States in Quantum Well

It is well known that the quantized states are formed in *n*-type quantum well structure which can be derived from a single conduction band structure. Within the framework of effective mass approximation, the quantized states can be solved from the one dimensional (1-D) time independent Schrödinger equation which is given by

$$\left[-\frac{\hbar^2}{2m^*}\frac{d^2}{dz^2}+V(z)\right]\phi_n(z)=E_n\phi_n(z) \tag{2.1}$$

where $\hbar = h/(2\pi)$, h is Planck's constant, m^* is the effective mass of electron, $V(z)$ is the potential function, ϕ_n is the wavefunction of electron, and E_n is the energy level. Using the Kronig-Penney model, the envelope wavefunction ϕ_n can be written as [24]

$$\phi_n(z)=\begin{cases} C_1\cos\left[k_w\left(z-\frac{L_w}{2}\right)\right]+C_2\sin\left[k_w\left(z-\frac{L_w}{2}\right)\right], \text{ in the well} \\ C_3\cos\left[k_b\left(z+\frac{L_b}{2}\right)\right]+C_4\sin\left[k_b\left(z+\frac{L_b}{2}\right)\right], \text{ in the barrier} \end{cases} \tag{2.2}$$

where

$$k_w=\frac{2m_w^*\left(E-V_w\right)^{1/2}}{\hbar}, \tag{2.3}$$

$$k_b=\frac{2m_b^*\left(E-V_b\right)^{1/2}}{\hbar}, \tag{2.4}$$

and $C_{1\text{-}4}$ are constants which depend on boundary conditions and subband index parity, $V_{w,b}$ are conduction band minima for the well and barrier layers, L_w and L_b are the width for the well and barrier layers, respectively.

Bastard [25] has shown that, in the parabolic band approximation, the dispersion relation for the unbound states is

$$\cos\left[k_z\left(L_w+L_b\right)\right]=\cos\left(k_wL_w\right)\cos\left(k_bL_b\right)-\frac{1}{2}\left(\frac{1}{\xi}+\xi\right)\sin\left(k_wL_w\right)\sin\left(k_bL_b\right) \tag{2.5}$$

with $\xi = m_b^*k_w / m_w^*k_b$ and k_z defines the superlattice wavevector. The dispersion relation for the bound states is still valid if one substitutes k_b by $i\kappa_b$ and ξ by $-i\xi'$ with $\xi' = m_b^*k_w / m_w^*k_b$,

$$\cos\left[k_z\left(L_w+L_b\right)\right]=\cos\left(k_wL_w\right)\cosh\left(\kappa_bL_b\right)-\frac{1}{2}\left(\frac{1}{\xi'}-\xi'\right)\sin\left(k_wL_w\right)\sinh\left(\kappa_bL_b\right) \tag{2.6}$$

The energy level of the bound states can then be solved from the above equations.

To solve the Schrödinger equation with an arbitrary potential function, many different approaches have been used [26-29] such as WKB approximation, Monte Carlo simulation, and variational method. Recently, the transfer matrix method (TMM) [11] has been developed to solve this problem faster than the other methods and shown to obtain the same results. Let us consider the multiple quantum well structure which consists of a narrow-bandgap quantum well sandwiched between two wider bandgap barrier layers as shown in Fig. 2.1. The solution of the Schrödinger equation in each of the multiple quantum-well and barrier regions consists of two components propagating in forward and backward directions, respectively. The total wavefunctions can be written as

$$\phi_i = A_i^+ e^{-i\Delta_i} e^{ik_i z} + A_i^- e^{i\Delta_i} e^{-ik_i z} \tag{2.7}$$

where

$$\begin{aligned} &\Delta_1 = \Delta_2 = 0, \\ &\Delta_i = k_i\left(d_2 + d_3 + \cdots + d_{i-1}\right); \quad i = 3,4,\cdots,N, \text{ and} \end{aligned} \tag{2.8}$$

$$k_i = \sqrt{\frac{2m^*\left(E - V_i\right)}{\hbar^2}} \tag{2.9}$$

where A_i^+ and A_i^- represent the magnitudes of the particle wave functions propagating along the +*z* and -*z* directions, respectively, and *N* is the total number of layer regions. Since ϕ and $d\phi/dz$ are continuous at the boundaries, we obtain

$$A_i^+ = \frac{e^{i\delta_i} A_{i+1}^+ + r_i e^{i\delta_i} A_{i+1}^-}{t_i}, \tag{2.10}$$

$$A_i^- = \frac{r_i e^{-i\delta_i} A_{i+1}^+ + e^{-i\delta_i} A_{i+1}^-}{t_i} \tag{2.11}$$

here the recurrence relation may be written in matrix form

$$\begin{pmatrix} A_i^+ \\ A_i^- \end{pmatrix} = \frac{1}{t_i} \begin{pmatrix} e^{i\delta_i} & r_i e^{i\delta_i} \\ r_i e^{-i\delta_i} & e^{-i\delta_i} \end{pmatrix} \begin{pmatrix} A_{i+1}^+ \\ A_{i+1}^- \end{pmatrix} \tag{2.12}$$

where

$$\begin{aligned} r_i &= \frac{(m^*_{j+1}/k_{j+1}) - (m^*_j/k_i)}{(m^*_{j+1}/k_{j+1}) + (m^*_j/k_i)}, \\ t_i &= \frac{2(m^*_{j+1}/k_{j+1})}{(m^*_{j+1}/k_{j+1}) + (m^*_j/k_i)}, \text{ and} \\ \delta_i &= k_i d_i. \end{aligned} \tag{2.13}$$

Thus, we have

$$\begin{pmatrix} A_1^+ \\ A_1^- \end{pmatrix} = S_1 \begin{pmatrix} A_2^+ \\ A_2^- \end{pmatrix} = S_1 S_2 \begin{pmatrix} A_3^+ \\ A_3^- \end{pmatrix} = \cdots = S_1 S_2 \cdots S_{N-1} \begin{pmatrix} A_N^+ \\ A_N^- \end{pmatrix}. \tag{2.14}$$

Since there is no backward propagating component in the last medium, i.e. $A_N^- = 0$, one can find $A_j^+ (j = 2,3,\cdots,N)$ in term of A_1^+, where j represents the layer region to be investigated. The transmission coefficient T_x is then given by $|A_N^+ / A_1^+|^2$. If we calculate the transmission coefficient as a function of E, then we can obtain certain resonance peaks. It can be shown that the resonance curve is Lorentzians distribution which corresponds to each bound state and quasi-bound state of the form

$$T_x = \left|\frac{A_N^+}{A_1^+}\right|^2 = \frac{T_p (\Gamma/2)^2}{(E - E_p)^2 + (\Gamma/2)^2} \tag{2.15}$$

where E_p is the energy of the resonance peak, and Γ is the full width at half maximum (FWHM). Due to heavily doped quantum well in *n*-type QWIPs, there are some extra terms that should be included in calculations of electron states, such as electron-electron intrasubband exchange and direct Coulomb interaction energies, depolarization effect, and exciton-like shifts [30]. Of these terms, the effect due to the electron-electron intrasubband exchange energy is dominated within the doping density from 5×10^{16} cm^{-3} to 3×10^{18} cm^{-3}. Bandara et al. [31] first presented experimental evidence for an exchange-induced shift in the peak response of QWIP. The exchange interaction term associated with an electron in the ground state due to all other electrons in the subband can be written as [32]

$$E_{exch}(0) \approx -\frac{q^2 k_F}{4\pi\,\varepsilon}\left[1 - 0.31\frac{k_F}{k_1}\right],$$
$$E_{exch}(k_F) \approx -\frac{q^2 k_F}{4\pi\,\varepsilon}\left[\frac{2}{\pi} - 0.31\frac{k_F}{k_1}\right] \qquad (2.16)$$

where $k_1 = \pi / L_w$, $k_F = 2\pi\,\sigma^{1/2}$, ε is the dielectric constant, $\sigma = L_w N_d$ is the two-dimensional electron density in the quantum well, and N_d is the doping density in the quantum well.

2.3 Strain Effects on the Energy Bandgap

Recently, there has been a considerable interest in the development of strained-layer QWIPs [33-37]. Strained-layer heterostructures allow the use of lattice-mismatched materials without the generation of misfit dislocations if the layer thickness is less than the critical thickness [38]. This freedom from the need for precise lattice matching widens the choice of compatible materials and greatly increases the ability to control the electronic and optical properties of the strained-layer structures.

Strain effects induced by lattice-mismatch will modify the energy band structure. From the elasticity theory [39], the biaxial strain can be divided into two independent components: one is isotropic or hydrostatic component and the other is anisotropic or shear uniaxial component. The strain-induced energy shifts, ΔE_H due to the hydrostatic component and ΔE_U due to the shear uniaxial component, can be expressed, respectively, by [40]

$$\Delta E_H = 2V_{cd}\frac{C_{11} - C_{12}}{C_{11}}\delta_0,$$
$$\Delta E_U = V_{sd}\frac{C_{11} + 2C_{12}}{C_{11}}\delta_0 \qquad (2.17)$$

where V_{cd} and V_{sd} are the conduction-band deformation potential and shear deformation potential, respectively, C_{ij} are the elastic constants, and δ_0 is the lattice-mismatch strain, $\delta_0 = (a_s - a)/a$ where a_s and a are the lattice constants of the substrate and the strained-layer, respectively. The energy bandgaps due to the strain for the heavy-hole and light-hole states at $k = 0$ are given by [40]

$$\begin{aligned} \left(E_g^{C,HH}\right)_s &= \left(E_g^0\right)_s + \Delta E_H - \Delta E_U, \\ \left(E_g^{C,LH}\right)_s &= \left(E_g^0\right)_s + \Delta E_H + \Delta E_U - \frac{\left(\Delta E_U\right)^2}{2\Delta_o} + \cdots \end{aligned} \qquad (2.18)$$

where $(E_g^0)_s$ is the unstrained bandgap and Δ_o is the spin-orbit splitting energy. The bandoffsets of the conduction and valence band of the heterostructure can be calculated by

$$\begin{aligned} \Delta E_C &= Q_C \Delta E_g, \\ \Delta E_V &= Q_V \Delta E_g \end{aligned} \qquad (2.19)$$

where Q_C and Q_V are the band offset ratios of the conduction and valence bands, respectively, and ΔE_g is the energy gap discontinuity of the barrier and well materials.

2.4 Intersubband Transition

For intersubband absorption, doping is very important to provide the carriers for the ground state in the quantum well. Quantum confinement of carriers in a semiconductor quantum well leads to the formation of quantized energy levels and the drastic change of optical absorption spectral. One of the most remarkable properties of these quasi-two-dimensional (2-D) electronic systems is that the optical transitions between the quantized states are feasible. The linear intersubband transitions within the conduction band have been studied experimentally without an electric field [7, 41] and with an electric field [8]. A very large dipole strength and a narrow band width were observed. Absorption coefficient studies are of great importance for QWIPs because of their direct connection to the design of QWIP's parameters such as the detecting wavelength, quantum efficiency, and photoresponse. Theoretical calculations for interband [42] and intersubband transitions [43] in quantum wells have been reported. Self-consistent solutions have also been used for multiple quantum wells and superlattice [44, 45] for the subband structure.

The linear intersubband absorption coefficient within the conduction band of the quantum well can be expressed as [46]

$$\alpha(\omega) = \omega\sqrt{\frac{\mu_0}{\varepsilon}}\left(\frac{q^2 m^* kT}{L_w \pi \hbar^2}\right)\sum_{m>n}\left[|M_{mn}|^2 \times \ln\left(\frac{1+\exp[(E_F-E_n)/kT]}{1+\exp[(E_F-E_m)/kT]}\right) \times \frac{(\hbar/\tau)^2}{(E_m-E_n-\hbar\omega)^2+(\hbar/\tau)^2}\right] \tag{2.20}$$

where μ_0 is the permeability in vacuum, ε the dielectric constant, L_w the total quantum well width, τ the lifetime, E_F the Fermi level of the system. The dipole matrix element M_{mn} is given by

$$M_{mn} = \int_{-L_w/2}^{L_w/2} \phi_m^*(z)|z|\phi_n(z)\,dz. \tag{2.21}$$

The integrated absorption strength is given by

$$I_A = \int_0^\infty \alpha(w)\,dw \tag{2.22}$$

and the dipole oscillator strength is given by

$$f_{os} = \frac{4\pi m^* c}{\hbar\lambda}|M_{mn}|^2. \tag{2.23}$$

The Fermi level E_F can be calculated from [22]

$$N_d = \frac{m^* kT}{\pi \hbar^2 L_w}\sum_n \ln\left[1+\exp\left(\frac{E_F-E_n}{kT}\right)\right]. \tag{2.24}$$

It is noted that N_d expression is valid for summation over subband levels E_n below the Fermi level E_F. It is noted from equation (2.21) that the normal incidence radiation for *n*-type QWIPs will not be absorbed because there is no electric field component along the *z*-axis. Therefore, both 45° polished facet illumination and grating coupler [47-49] have been used to characterize the performance of the *n*-type QWIPs as shown in Fig. 2.2.

2.5 Performance of the Quantum Well Infrared Photodetectors

Calculations of the dark current for a standard QWIP have been reported by Levine et al. [50]. Under dark conditions, electrons can transfer out of the quantum wells and produce the dark current via three main mechanisms: thermionic emission, thermally assisted tunneling, and direct or trap-assisted tunneling as shown in Fig. 2.3. In the low-field regime and at higher temperature, the dark current is dominated by the thermionic emission, which can be expressed as [23]

$$I_d = A_d q v_d n_t \qquad (2.25)$$

where A_d is the detector active area, q is the electron charge, and

$$\begin{aligned} v_d &= \frac{\mu_e F}{(1+(\mu_e F / v_s)^2)^{1/2}}, \\ n_t &= m^* kT\pi \hbar^2 L_w e^{-(E_{co}-E_F)/(kT)}. \end{aligned} \qquad (2.26)$$

Here μ_e is the electron mobility, F is the electric field, v_s is the saturation drift velocity, E_{co} is the cutoff energy related to the cutoff wavelength λ_c, $m^*/(\pi \hbar^2)$ is the 2-dimensional (2-D) density of states.

The conventional theory of photoconductivity is normally employed to describe QWIPs. The current responsivity is defined by the ratio of the photocurrent to the input optical power, i.e.

$$R_i = \frac{e}{h\nu}\eta g \qquad (2.27)$$

where η $(= (1/2)(1-R_f)(1-e^{-m\alpha l}))$ is the quantum efficiency, m is the number of absorption pass, g is the optical gain, R_f is the reflection coefficient, α is the absorption coefficient for the active QW layers, and l is the total thickness of the active layers. The optical gain can be expressed as [51]

$$g = \frac{I_d}{qN_{qw} A_d L_w \overline{G}} \qquad (2.28)$$

where I_d is the dark current, N_{qw} is the number of quantum wells, A_d is the detector area, L_w is the well width, and $\overline{G}$ is the thermal carrier generation rate density, which is given by

$$\overline{G} = N_d v_{th} \sigma_c N_C e^{-E_b/(kT)} = C_1 N_d \text{ cm}^{-3}\text{s}^{-1} \tag{2.29}$$

where N_d is the doping density, v_{th} is the thermal velocity, σ_c is the cross-sectional area for electron trapping into the quantum well ground state, N_c is the effective density of the conduction band states, and E_b is the barrier height.

Finally, the most important figure of merit, the specific detectivity D*, for IR detectors, should be discussed. The non-BLIP (Background Limited Performance) peak detectivity is determined [52] using

$$D_p^* = \frac{R_{i,p}\sqrt{A_d \Delta f}}{i_n} \tag{2.30}$$

where $R_{i,p}$ is the peak current responsivity, A_d is the detector area, Δf is the noise spectral bandwidth, and i_n is the overall root-mean-square noise current for a QWIP. The noise current consists of two components: one is the device's noise current i_{nd} and the other is the background photon noise current i_{nb}. There are two main subcomponents in the device's noise current: one is the G-R noise and the other is the Johnson noise, which are dominated in the PC mode and PV mode detection, respectively.

The BLIP peak detectivity is determined [50] using

$$D_{BLIP}^* = \frac{1}{2}\sqrt{\frac{\eta}{h\nu I_{BG}}} \tag{2.31}$$

where η is the net quantum efficiency, ν is the photon frequency, and I_{BG} is the intensity of the incident background, which can be expressed as

$$I_{BG} = \sin^2\left(\frac{\Omega}{2}\right)\cos(\theta)\int_{\lambda_1}^{\lambda_2} W(\lambda)\, d\lambda \tag{2.32}$$

where Ω is the field of view (FOV), θ is the incident angle, λ_1 and λ_2 are the lower-bound and upper-bound wavelength in the spectral region of the detector, respectively, and $W(\lambda)$ is the blackbody spectral density given by Planck's blackbody radiation formula

$$W(\lambda) = \frac{2\pi c^2}{\lambda^5} \frac{1}{e^{hc/\lambda kT_{BG}} - 1} \tag{2.33}$$

where c is the speed of light, λ is the wavelength, h is Planck's constant, k is Boltzman's constant, and T_{BG} is the temperature of the background.

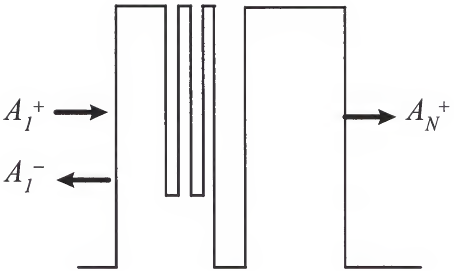

Figure 2.1. The schematic conduction band diagram of a multiple quantum well, with arbitrary well width and height.

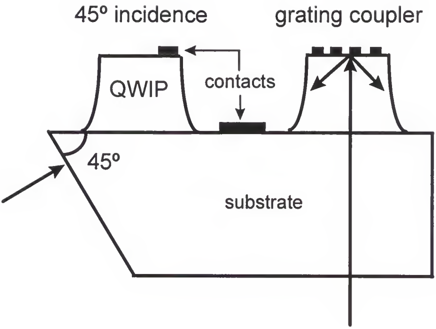

Figure 2.2. The coupling methods for *n*-type direct gap QWIPs: 45° incidence and grating coupler.

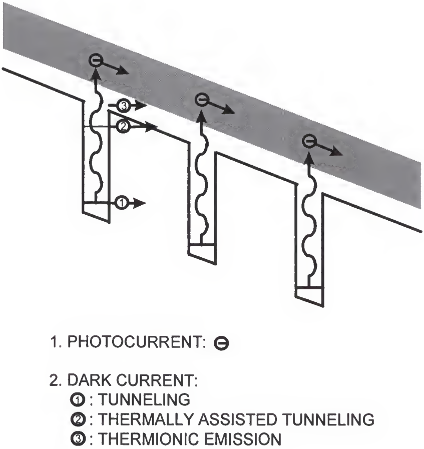

Figure 2.3. The photocurrent and dark current components in *n*-type QWIPs.

CHAPTER 3

A GAAS/ALAS/ALGAAS AND GAAS/ALGAAS STACKED QUANTUM WELL INFRARED PHOTODETECTOR FOR 3 – 5 AND 8 – 14 μm DETECTION

3.1 Introduction

In this chapter we demonstrate a new two-color stack GaAs/AlAs/AlGaAs and GaAs/AlGaAs QWIP with PV and PC dual-mode operation at 3 – 5 and 8 – 14 μm. Recently, quantum well infrared photodetectors (QWIPs) [9, 11, 53, 54] have been used in the infrared focal plane arrays (FPAs) imaging sensor systems [55]. Furthermore, multicolor and voltage-tunable QWIPs have been achieved [14, 17, 18] using multistack, asymmetric and symmetric quantum well structures. Most of the QWIPs are operating on the photoconductive (PC) mode detection. However, significant photovoltaic (PV) effects in the QWIPs have also been reported in the literature [19, 56, 57]. The PV mode operation is promising for practical applications, since the suppression of the dark current strongly improves the noise properties. However, the responsivity of the PV mode in a typical QWIP is significantly smaller than that of the PC mode. Therefore, improvement in the performance of PV QWIPs is highly desirable for using such detectors in the infrared FPA image sensor applications.

3.2 Device Growth and Fabrication

The QWIP layer structure was grown on a semi-insulating (SI) GaAs substrate by using the molecular beam epitaxy (MBE) technique. This 2-color QWIP consists of a GaAs/AlGaAs QWIP for long-wavelength infrared (LWIR) detection stacked on top of the GaAs/AlAs/AlGaAs QWIP for mid-wavelength infrared (MWIR) detection.

Figure 3.1 shows the device structure of this 2-color stacked QWIP. A 0.7 μm GaAs buffer layer (doped to $n = 2.0\times10^{18}$ cm^{-3}) was first grown on the SI GaAs substrate as an ohmic contact layer, followed by the growth of the first stack, designed as a MWIR-QWIP with a 20-period of GaAs/AlAs/AlGaAs double barrier quantum wells (DBQW) [49] with a well width of 5 nm (doped to $n = 1.5\times10^{18}$ cm^{-3}) and two undoped barriers which were of 1.4 nm AlAs inner barrier and 30 nm $Al_{0.3}Ga_{0.7}As$ outer barrier. A second GaAs buffer layer of 0.5-μm thick (doped to $n = 2.0\times10^{18}$ cm^{-3}) was then grown on top of the first QWIP as an ohmic contact layer, followed by the growth of the second stack, designed as a LWIR-QWIP, with a 21-period of GaAs/AlGaAs quantum wells with a well width of 8.8 nm and a dopant density of 1.5×10^{18} cm^{-3}. The barrier layer on each side of the GaAs quantum wells consists of a 8-period undoped $Al_{0.3}Ga_{0.7}As$ (5 nm)/GaAs (2.8 nm) superlattice layer which were grown alternatively with the GaAs quantum wells. Finally, an n^+-GaAs cap layer of 0.3 μm thick with a dopant density of $n = 2.0\times10^{18}$ cm^{-3} was grown on top of the QWIP layer structure to facilitate the top ohmic contact. The DBQW structure of the MWIR-QWIP offers a PV mode detection with excellent detection characteristics which are comparable to the PC mode QWIPs. The physical parameters of the LWIR-QWIP are chosen so that the first excited level E_2 is lined up within the miniband E_{SL} on both sides of the quantum well to obtain a maximum intersubband absorption strength. In order to minimize the undesirable tunneling current through the barrier layers, a 8-period undoped $Al_{0.3}Ga_{0.7}As$(5-nm)/GaAs(2.8-nm) superlattice layer was used in this LWIR-QWIP structure to suppress the tunneling current from the heavily populated ground state E_1 in the quantum wells.

The 2-color QWIP mesa structure with an active area of 200×200 μm^2 was created by chemical etching through the two-stack quantum well active layers and stopped at the 0.7-μm thick heavily doped GaAs buffer layer for ohmic contact. A square contact ring composed of AuGe/Ni/Au materials was first deposited around the periphery of the mesa and alloyed for ohmic contact formation. To enhance the light coupling efficiency in the quantum well, we used a 2-D double periodic square mesh metal grating coupler [48] on the QWIP for normal incident illumination with $g = 4$ μm(where g is the grating period) and $a/g = 0.5$ (where a is the width of square aperture in the metal mesh). The metal grating was then deposited within the interior of the contact ring by using electron beam evaporation of Au followed by lift-off process.

3.3 Results and Discussion

Figure 3.2(a) and (b) show the energy band diagrams of this 2-color QWIP structure, which illustrate the bound-to-quasi-bound (BTQB) and the bound-to-miniband (BTM) transition schemes for the 2-color detection, respectively. The first transition scheme is from the localized ground-state E_1 to the first quasi-bound state E_2 in the GaAs quantum well of the MWIR-QWIP, as shown in Fig. 3.2(a). The second transition scheme is from the localized ground-state E_1 to the miniband E_{SL} in the GaAs quantum well of the LWIR-QWIP (Fig. 3.2(b)). To analyze these transition schemes, we performed theoretical calculations of the energy levels of the bound states and continuum states and the transmission probability $|T^*T|$ for this detector using a multi-layer transfer matrix method [11] and the results are shown in Fig. 3.3. Considering only the effects due to depolarization and the electron-electron interaction [32], we obtain two response peaks, one at $\lambda = 3.9$ μm and the other at $\lambda = 11.7$ μm.

To understand the behavior of this 2-color QWIP, we first prepared two samples with BTQB and BTM quantum structures discussed above separately. The MWIR-QWIP (BTQB) and LWIR-QWIP (BTM) represent the first stack and the second stack of this 2-color QWIP structure, respectively. Figure 3.4(a) shows the dark current versus bias voltage (I–V) curves of the MWIR-QWIP and the LWIR-QWIP measured at $T = 50$ and 77 K, respectively. The results show that the dark current of the LWIR-QWIP is higher than that of the MWIR-QWIP at the same bias. This is due to the fact that the LWIR-

QWIP has a smaller barrier and the thermionic-generated electrons can escape more easily from the quantum wells. Therefore, based on the *I–V* curves shown in Fig. 3.4(a), we can see that when the two stacks are combined to form a 2-color detector, most of the voltage drop will be across the MWIR-QWIP stack at low bias ($V_b < 1.5$ V). Therefore, a high field domain always forms first in the MWIR-QWIP stack. The voltage drop across the LWIR-QWIP stack becomes significant only when the bias is greater than 1.5 V. Figure 3.4(b) shows the total dark current-voltage (*I–V*) for the 2-color stacked QWIP measured at $T = 50$ and 77 K, respectively. It is noted that the 300 K background photocurrent curve (dashed) crosses the dark *I–V* curve at $V_b = -0.65$ V and $T = 50$ K. Thus, the background limited performance (BLIP) condition occurs at $T \leq 50$ K and $V_b \leq$ 0.65 V. The 300 K background photocurrent can be obtained from

$$I_B = \int_{\lambda 1}^{\lambda 2} R(\lambda) S(\lambda)\, d\lambda$$

where A is the device area, $R(\lambda)$ is the responsivity curve, λ_1 and λ_2 are the wavelengths of the lower and upper limits of the integration, and the blackbody power spectral density is given by

$$S(\lambda) = \left(2\pi\, hc / \lambda^5\right)\left(e^{hc/\lambda kT} - 1\right)^{-1}.$$

Using $A = 4\times10^{-4}$ cm^2, $R_p = 0.018$ A/W (at $\lambda = 4.1$ μm, $V_b = 0$ V, and $T = 30$ K), and $T = 300$ K gives a total calculated 300 K background photocurrent of $I_B = 0.12$ nA. This is in good agreement with the measured photocurrent of $I_B = 0.3$ nA (as shown in Fig. 3.4(b)). Therefore, at $T = 50$ K this 2-color detector is under BLIP condition only in the PV mode operation, but not the PC mode operation.

The spectral response of the 2-color QWIP was measured under back illumination as a function of temperature and bias voltage (V_b) using a 0.25 m grating monochromator with a 1000 °C blackbody source. The normalized spectral responsivity measured at $V_b =$ 0, 3.2 V and $T = 50$ K is shown in Fig. 3.5(a). Two response peaks were observed: one at

λ = 4.1 μm with V_b = 0 V and the other at λ = 11.6 μm with V_b = 3.2 V. The peak wavelengths are in good agreement with our theoretical calculations. The bias dependence of the responsivity at T = 50 K is shown in Fig. 3.5(b). It is noted that the photoresponse of the MWIR-QWIP is dominated at low bias and saturated above V_b = 1 V. The LWIR-QWIP takes over for V_b > 2.5 V and reaches a maximum value at V_b = 3.2 V. The results show the potential of this 2-stack QWIP structure as a 2-color QWIP with a PV and PC dual-mode operation at 3-5 μm and 8-14 μm. The peak responsivity at zero bias (PV mode) was found to be 17 mA/W at λ = 4.1 μm and T = 50 K, with a bandwidth $\Delta\lambda/\lambda_p$ = 15 %. Two peak responsivities were found on the PC mode, one was 25 mA/W at λ_p = 4.1 μm, V_b = 1.0 V, and T = 50 K, the other was 0.12 A/W at λ_p = 11.6 μm, V_b = 3.2 V, T = 50 K, and the bandwidth $\Delta\lambda/\lambda_p$ = 18 %. The PV responsivity was found to be 68 % of the PC responsivity at λ_p = 4.1 μm and T = 50 K and we obtained the same ratio in the MWIR-QWIP. This is the highest ratio reported for the spectral region of 3 – 5 μm wavelength with a DBQW structure. The PV response has been interpreted due to the doping migration effect [56] with further enhancement by the DBQW structure. Since the dark current of the PV mode operation QWIP is much smaller than that of the PC mode, one can achieve a better performance in QWIP by using PV mode detection at 3 – 5 μm.

3.4 Conclusions

In conclusion, we have demonstrated a new two-color stacked GaAs/AlAs/AlGaAs BTQB QWIP and GaAs/AlGaAs BTM QWIP with PV and PC dual-mode operation at 3 – 5 and 8 – 14 μm. The PV detection scheme uses transition from the ground-state to the quasi-bound state of the MWIR-QWIP. The PC detection scheme has two different transitions, one is similar to the PV detection scheme and the other uses transition from the ground-state to the miniband of the LWIR-QWIP. The peak responsivity at zero bias (PV mode) was found to be 17 mA/W at λ_p = 4.1 μm, T = 50 K, with a $\Delta\lambda/\lambda_p$ = 15 %.

Two peak responsivities for the PC mode detection, were found to be 25 mA/W at λ_p = 4.1 μm, V_b =1 V, and T = 50 K, and 0.12 A/W at λ_p = 11.6 μm, V_b =3.2 V, T = 50 K, and the bandwidth $\Delta\lambda/\lambda_p$ = 18 %. The PV responsivity was found to be 68 % of the PC responsivity at λ_p = 4.1 μm and T = 50 K, demonstrating the ability for an efficient PV mode operation at 3 – 5 μm. Further improvement on the performance of the 2-color QWIP is expected to raise the operating temperature to T = 77 K for practical focal plane arrays image sensor applications.

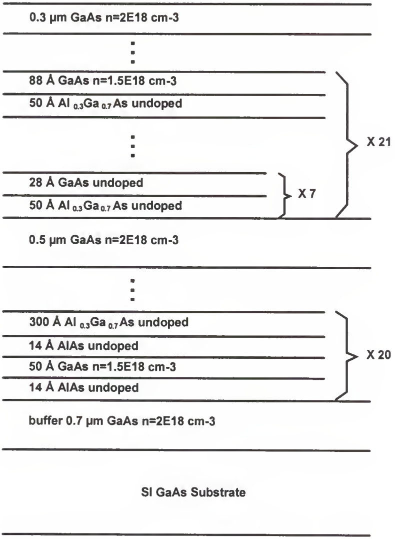

Figure 3.1. The layer structure of the two-stack two-color DB/BTM QWIP.

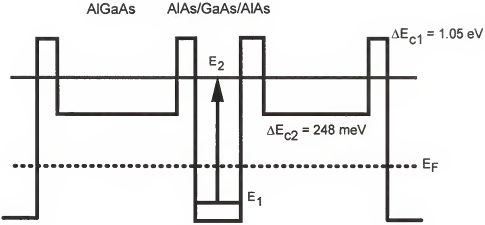

(a) MWIR-QWIP stack

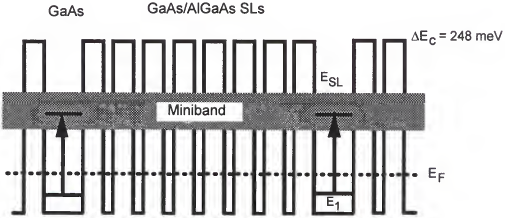

(b) LWIR-QWIP stack

Figure 3.2. The schematic conduction band diagrams for the two-stack two-color DB/BTM QWIP: (a) MWIR-QWIP and (b) LWIR-QWIP.

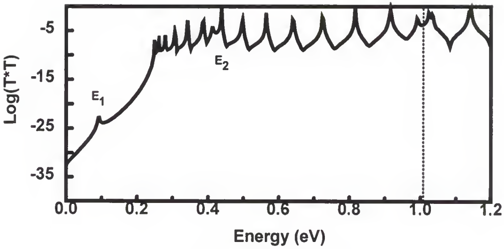

(a) MW-QWIP stack

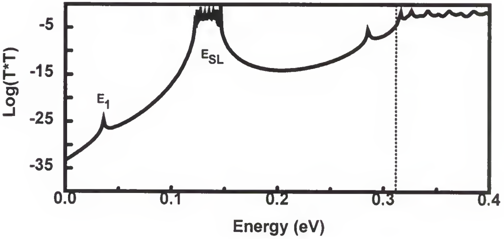

(b) LW-QWIP stack

Figure 3.3. The transmission coefficients of the two-stack two-color DB/BTM QWIP: (a) MW-QWIP stack and (b) LW-QWIP stack.

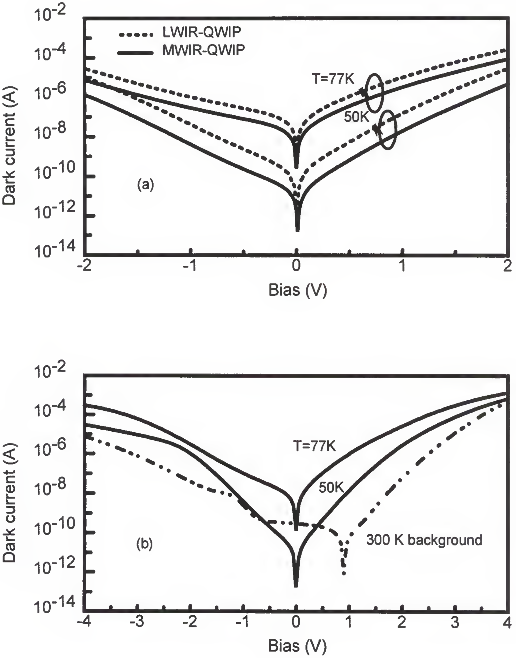

Figure 3.4. The dark current vs bias voltage measured at $T = 50$ and 77 K for (a) the LWIR-QWIP and the MWIR-QWIP and (b) the two-color MWIR and LWIR stacked QWIP.

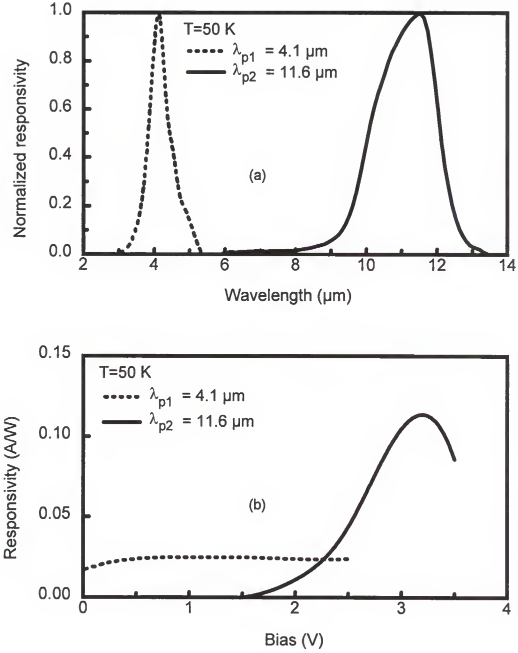

Figure 3.5. (a) Normalized responsivity vs wavelength and (b) peak responsivity vs bias for the two-stack two-color DB/BTM QWIP measured at $T = 50$ K.

CHAPTER 4

A VOLTAGE-TUNABLE MULTICOLOR TRIPLE-COUPLED INGAAS/GAAS/ALGAAS QUANTUM WELL INFRARED PHOTODETECTOR FOR 7 – 14 μm DETECTION

4.1 Introduction

Quantum well infrared photodetectors (QWIPs) based on bound-to-bound (BTB) states, bound-to-continuum (BTC), and bound-to-miniband (BTM) transitions have been widely investigated in recent years for 8 – 14 μm atmospheric window detection [11, 12, 41]. High performance focal plane arrays (FPAs) based on GaAs/AlGaAs BTC and BTM QWIPs (with peak wavelength at 9 – 9.5 μm) have been demonstrated for LWIR imaging applications [23, 55, 58, 59, 60]. Using bandgap engineering, a wide variety of multicolor QWIPs such as voltage-tunable multicolor QWIPs and multistack quantum well structures for detection in both mid-wavelength infrared (MWIR) and long-wavelength infrared (LWIR) bands have been published [17, 20, 61, 62, 63, 64].

The Use of coupled asymmetric quantum wells for multicolor detection has been developed [20], but strong Stark shift has not been observed in the coupled two quantum wells structure. Recently, Huang and Lien [65] have proposed a two-depth three coupled quantum well (TCQW) and its application for a voltage-tunable IR detector. Based on their theoretical calculations, they predicted a very large Stark shift offset with wavelength tunability in 7 – 14 μm by an applied bias voltage for the two-depth TCQW structure. This wavelength tunability is very useful in military application such as target discrimination.

In this chapter we report the development of two voltage-tunable multicolor triple-coupled quantum well infrared photodetectors (TC-QWIPs) for 7 – 14 μm detection. The wavelength tunability is achieved in the 8.2 – 9.1 μm and 10.8 – 11.5 μm for two different TC-QWIP structures. Using the strongly coupled quantum well structure, multicolor detection is achieved in the 7 – 12 μm under different bias voltages and polarity conditions.

4.2 Device Growth and Fabrication

The layer structures of the TC-QWIP- A and B are shown in Fig. 4.1. These two TC-QWIP structures were grown on semi-insulating GaAs substrates by using molecular beam epitaxy (MBE) technique. The basic structure consists of a triple-coupled, symmetric quantum well (TCQW) separated by two thin $Al_yGa_{1-y}As$ barriers, and a 50 nm $Al_yGa_{1-y}As$ barrier (y = 0.21, 0.19 for QWIP- A and B, respectively), which was repeated 20 times to form the QWIP device. The TCQW is composed of a Si-doped ($N_d = 5\times10^{17}$ cm^{-3}) $In_xGa_{1-x}As$ deep well (x = 0.06, 0.03 and width = 6, 8 nm for QWIP- A and B, respectively) and two undoped GaAs shallow wells (width = 3 and 3.5 nm for QWIP- A and B, respectively) separated by two 1.6 nm $Al_yGa_{1-y}As$ thin barriers. Heavily doped ($N_d = 2\times10^{18}$ cm^{-3}) GaAs layers were grown for the top and bottom ohmic contacts.

4.3 Results and Discussion

A mesa structure with an active area of 200×200 μm^2 was formed for the TC-QWIP by chemical etching to facilitate for the device characterization. A square contact ring composed of AuGe/Ni/Au was first deposited around the periphery of the mesa and alloyed for ohmic contacts. The devices were then processed with both 45° polished facet and 2-D grating coupler for coupling IR radiation.

Figure 4.2 shows the schematic band diagram of the conduction-band and the bound-state energy levels for a TC-QWIP under positive bias condition. For the TC-QWIP, due to the strong coupling effect of the three asymmetrical QWs and two thin

AlGaAs barriers, the bound states in the GaAs QWs and the first excited state in the InGaAs QW are coupled to form the second (E_2) and third (E_3) bound states inside the TCQWs under applied bias condition, as illustrated in Fig. 4.2. The intersubband transition for the TC-QWIP is dominated by the bound-to-bound transition between E_1 and E_3 states, while two secondary photoresponse peaks due to $E_1 \rightarrow E_2$ and $E_1 \rightarrow E_C$ states transitions were also observed in the TC-QWIP under large bias condition. To calculate the energy levels in the TCQWs, the effects of electron-electron interaction [32] and strain-induced energy shift [39] in the $In_xGa_{1-x}As$ layer was considered (this effect was neglected in Ref.[65]). Using multilayer transfer matrix method (TMM), the energy levels of the bound states and continuum states were calculated which are shown in Fig. 4.3. The calculated values of the conduction-band offset (ΔE_C = 212 and 163 meV for QWIP-A and -B, respectively) were found in excellent agreement with the measured values (ΔE_C = 220 and 165 meV) determined from the activation energy of the dark current versus inverse temperature plot at low bias for both devices as shown in Fig. 4.4. The calculated peak wavelengths for $E_1 \rightarrow E_3$ transition under zero bias are 9.4 μm and 11.5 μm [$E_{13} = (E_3 - E_1)$ = 132 and 109 meV], which were found in excellent agreement with the values of 9.3 μm and 11.7 μm obtained from Figs. 4.6(a) and 4.6(b) for QWIP-A and -B, respectively.

The dark current density versus bias voltage (J_d vs V_b) curves measured at T = 31 to 77 K for QWIP-A and -B are shown in Figs. 4.5(a) and 4.5(b), respectively. Both devices showed the asymmetric dark current characteristics under the positive and negative bias conditions, which are attributed to the asymmetric potential barriers in the TCQW structure. Since the effective barrier height under negative bias is smaller than that of positive bias case, J_d is larger under negative bias than the positive bias condition. It is also noted that J_d for QWIP-A is much smaller than that of QWIP-B due to the larger conduction-band offset and shorter cutoff wavelength for the former. For comparison, the 300 K background photocurrent curves [with a 180° field of view (FOV)] are also included in Figs. 4.5(a) and 4.5(b) for QWIP-A and -B, respectively. The BLIP temperature was found to be 66 K up to 7 V and 50 K up to 5V for QWIP-A and B, respectively.

The spectral response curves of both devices were measured as a function of temperature and bias voltage using a 0.25 m grating monochromator with a calibrated blackbody source $T_b = 1000$ °C). The responsivities were found to be nearly independent of temperature up to 77 K. Figures 4.6(a) and 4.6(b) show the plots of responsivity versus wavelength for QWIP-A and B, respectively, under different bias conditions.

For QWIP-A three detection peaks at 11.5, 8.2 – 9.1, and 7.2 μm were observed under positive and negative bias voltages, which are attributed to the transitions from the ground bound state to the first excited, second excited, and continuum states, respectively. Under positive bias, both $E_1 \rightarrow E_2$ and $E_1 \rightarrow E_3$ transitions were observed. The photoresponse due to ($E_1 \rightarrow E_3$) transition was observed for $V_b \geq 2.5$ V, which was due to the increase of the transmission probability of electrons from E_3 level. The peak responsivity was found to be 0.08 A/W at $\lambda_p = 8$ μm and $V_b = 7$ V. The bias dependence of the peak responsivity and wavelength were plotted in Figs. 4.6(a) and 4.6(b), which exhibit a linear dependence on the applied bias voltage, V_b. The responsivity data of the 2-D grating coupled device were also included along with the 45° facet incidence device, which showed a similar result. As shown in Fig. 4.6(a), the blue shift of ($E_1 \rightarrow E_3$) transition was due to the quantum-confined Stark effect in the asymmetric TCQW structure [65]. The tunable wavelength range of ($E_1 \rightarrow E_3$) transition was found to be 8.2 – 9.1 μm. The maximum BLIP detectivity, D^*_{BLIP}, was found to be 6.1×10^9 cm-Hz$^{1/2}$/W at $V_b = 5$ V, $\lambda_p = 8.6$ μm, FOV 180°, assuming a photoconductive gain of $g = 0.77$ [66]. In addition, the photoresponse due to ($E_1 \rightarrow E_2$) transition was observed for $V_b \geq 6$ V [see Fig. 4.6(a)]. However, under negative bias condition, only one detection peak at $\lambda = 7.2$ μm was observed at $V_b = -5.5$ V, which was attributed to the BTC states transition.

For QWIP-B, only two intersubband transition schemes, ($E_1 \rightarrow E_3$) and ($E_1 \rightarrow E_C$), were observed in the wavelength range from 6.5 μm to 13 μm. The coupling effect and the quantum-confined Stark effect described above are all applicable to QWIP-B. The ($E_1 \rightarrow E_2$) transition was beyond the wavelength of interest and was not measured in this study. Figure 4.6(b) shows the responsivity versus wavelength for QWIP-B, the photoresponse due to ($E_1 \rightarrow E_3$) transition was observed for $V_b \geq 2$ V. The peak responsivity was found to be 0.41 A/W at $\lambda_p = 11.0$ μm and $V_b = 5$ V. This value was an order of magnitude higher than that of QWIP-A for the ($E_1 \rightarrow E_3$) transition at $\lambda_p = 8.7$ μm. The peak detection wavelength versus bias voltage for QWIP-B is shown in the inset of Fig. 4.6(b), which also exhibits a linear dependence of the detection peak wavelength on the applied bias voltage. The tunable wavelengths for the ($E_1 \rightarrow E_3$) transition were found to be in the range of 10.8 – 11.5 μm. A maximum BLIP detectivity of $D^*_{BLIP} = 1.63\times10^{10}$ cm-Hz$^{1/2}$/W at $V_b = 4$ V, $\lambda_p = 11.2$ μm, FOV 180°, and $T_{BLIP} = 50$ K was obtained for this device, using a calculated photoconductive gain of $g = 0.6$ [66].

From the results presented above, it is noted that the main response peak for both QWIP- A and B devices is dominated by the ($E_1 \rightarrow E_3$) transition, while the photoresponse due to ($E_1 \rightarrow E_2$) transition only occurs under higher positive bias condition. The tunable range of the detection wavelengths were found to be 8.2 – 9.1 μm and 10.8 – 11.5 μm under positive bias condition for QWIP- A and B, respectively. The tunable wavelength range of QWIP-A was substantially smaller than that predicted by Huang and Lien [65]. One possible explanation could be attributed to the fact that they neglected the strain effects in the band offset calculations. As discussed above, the actual band offset of the TCQW was lower than that given in Ref. [65]. Thus, the tunable wavelength range should be smaller than that predicted in Ref. [65] when the strain effect is considered in the InGaAs quantum well.

4.4 Conclusions

In conclusion, we have demonstrated a new highly sensitive voltage-tunable multicolor triple-coupled quantum well infrared photodetector (TC-QWIP) for LWIR detection. Two TC-QWIP structures, QWIP- A and B, with different quantum well and barrier parameters have been fabricated and analyzed. Using quantum confined Stark shift effect, the wavelength tunability by the applied bias voltage in the wavelength range of 8.2 – 9.1 μm and 10.8 – 11.5 μm for QWIP- A and B, respectively, have been demonstrated in this work. Multi-wavelength photoresponses have been observed in both QWIP- A and B under different bias voltages and polarity conditions. As predicted by the theoretical calculations, the ($E_1 \rightarrow E_3$) transition is the dominant process responsible for the observed large photoresponsivity in both devices. Based on the results of this study, further optimization of the device parameters will be investigated in order to improve the performance of the TC-QWIPs for multicolor focal plane arrays (FPAs) applications.

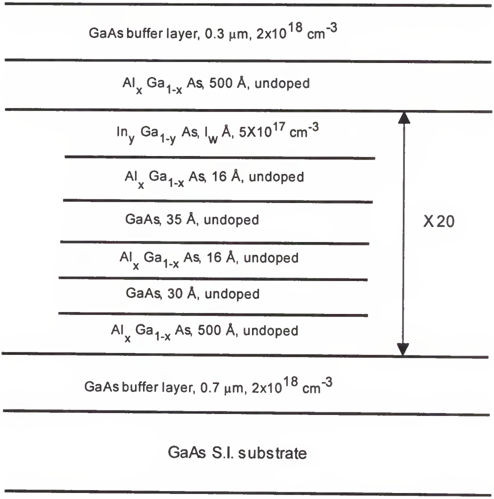
GaAs buffer layer, 0.3 μm, $2x10^{18}$ cm^{-3}
Al_x Ga_{1-x} As, 500 Å, undoped
In_y Ga_{1-y} As, l_w Å, $5X10^{17}$ cm^{-3}
Al_x Ga_{1-x} As, 16 Å, undoped
GaAs, 35 Å, undoped
Al_x Ga_{1-x} As, 16 Å, undoped
GaAs, 30 Å, undoped
Al_x Ga_{1-x} As, 500 Å, undoped
X20
GaAs buffer layer, 0.7 μm, $2x10^{18}$ cm^{-3}
GaAs S.I. substrate

Figure 4.1. The layer structure of the TC-QWIP: $x=0.21$, $y=0.06$, $l_w=60$ Å and $x=0.19$, $y=0.03$, $l_w=80$ Å for QWIP- A and B, respectively.

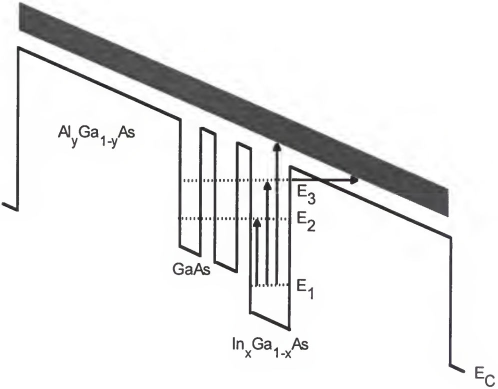

Figure 4.2. The schematic diagram of the conduction band for the TC-QWIP under positive bias conditions.

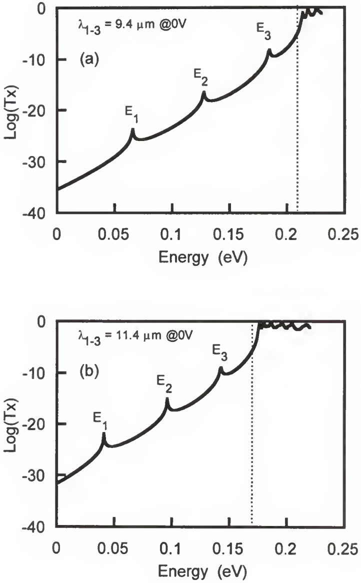

Figure 4.3. The transmission coefficients of the TC-QWIP A, (a), and the TC-QWIP B, (b).

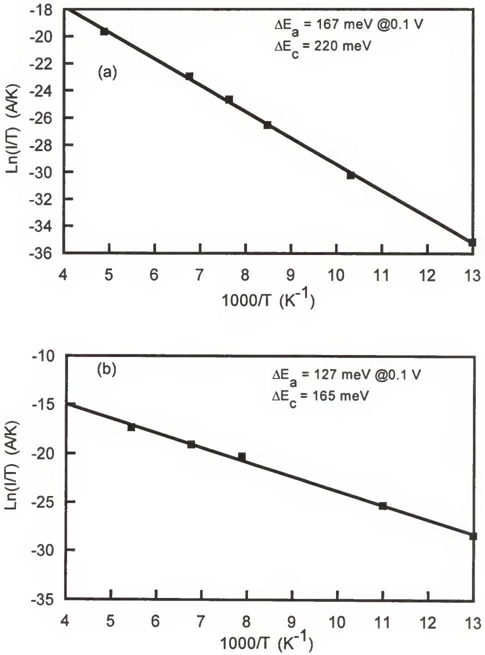

Figure 4.4. Arrehnius plot of the dark I-V for (a) QWIP-A and (b) QWIP-B, respectively.

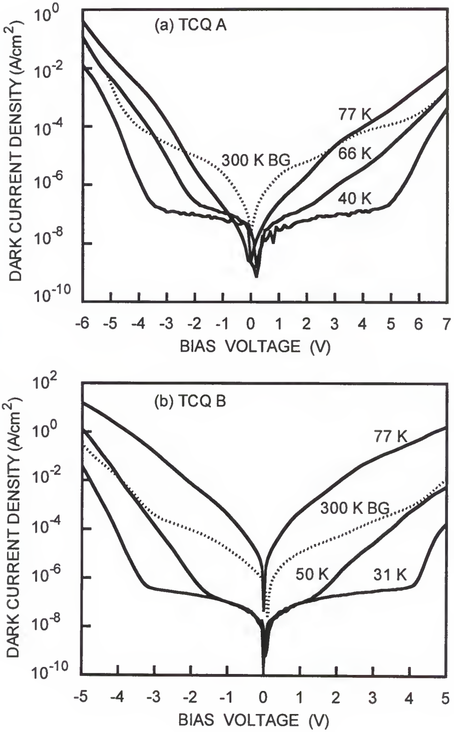

Figure 4.5. The dark current density versus bias voltage and temperature for (a) QWIP-A and (b) QWIP-B, respectively.

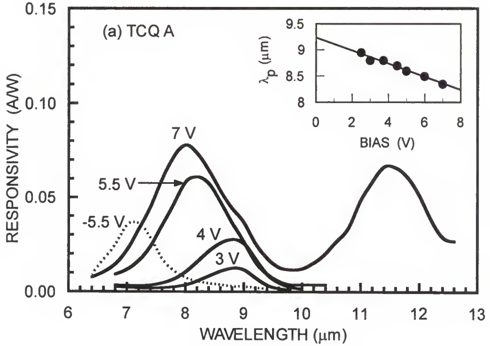

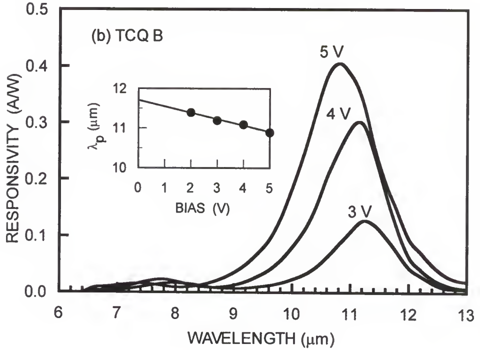

Figure 4.6. The responsivity versus wavelength for (a) QWIP-A and (b) QWIP-B. Strong Stark shift is clearly shown in (a) the 8-9 μm and (b) 11-12 μm range.

CHAPTER 5
A TWO-STACK TWO-COLOR HIGH STRAIN QUANTUM WELL INFRARED PHOTODETECTOR

5.1 Introduction

Quantum Well Infrared photodetectors (QWIPs) have been extensively investigated in recent years. One major feature of QWIP is its multicolor detection capability which is highly demanded by advanced infrared systems. Two-color detection that covers both of the 3 to 5 μm (MWIR) and 8 to 12 μm (LWIR) atmospheric windows is especially important in many applications. The primary concerns of the two-color detection are the difficulty of tuning the detection wavelength to the middle of the MWIR region and the low responsivity of the MWIR stack due to the narrow quantum wells. In this chapter, a high performance two-stack, two-color, high strain QWIP has been demonstrated. This QWIP was designed and provided by Dr. Tidrow of Army Research Laboratory. It consists of two stacks of multiple quantum wells (MQWs) as the active region with a highly doped contact layer in between the two stacks. The first stack consists of 20 periods of 30 nm $Al_{0.38}Ga_{0.62}As$ barrier and 2.4 nm doped $In_{0.35}Ga_{0.65}As$ well sandwiched between two 0.5 nm GaAs, and the second stack is composed of 20 periods of 50 nm $Al_{0.27}Ga_{0.73}As$ barrier and 5.5 nm GaAs well. Using two stacks for two-color detection have been reported before [17, 20, 63] but the indium concentration is limited to equal or less than 20 % in the InGaAs/AlGaAs MWIR stack due to the concern of the lattice mismatch induced strain problem. As a result, the quantum wells in the InGaAs/AlGaAs stack are not deep enough to cover the point of interest of the MWIR. Foire et al. [67] demonstrated an InGaAs/AlGaAs QWIP with 16 % indium and added two ultra thin AlAs barriers to the basic InGaAs/AlGaAs structure to push the excited state higher. We have developed a GaAs/AlAs/AlGaAs DB-QWIP [63] for the MWIR stack and achieved similar but better result as described in Chap. 3. However, the responsivity for both QWIPs in reference [63, 67] are very small due to the difficulty of confining the electron wavefunctions in the well region using the thin AlAs barriers. The dark current is also very high due to the easy tunneling of thermally excited electrons through the thin AlAs barriers. The device reported here incorporated 35 % of indium in the InGaAs well of the MWIR stack which achieved peak response at 4.3 μm with very low dark current and very high responsivity.

5.2 Device Growth and Fabrication

The schematic energy band diagram of the device is given in Fig. 5.1. It consists of two stacks of multiple quantum wells as the active region with a highly doped contact layer in between the two stacks. The first stack is designed to detect the MWIR which consists of 20 periods of 30 nm $Al_{0.38}Ga_{0.62}As$ barrier and 2.4 nm $In_{0.35}Ga_{0.65}As$ well sandwiched between two 0.5 nm GaAs. The second stack is for the LWIR detection which consists of 20 periods of 50 nm $Al_{0.27}Ga_{0.73}As$ barrier and 5.5 nm GaAs well. The doping densities are 2.5×10^{18} cm^{-3}, 0.7×10^{18} cm^{-3}, and 1×10^{18} cm^{-3} for the MWIR stack, LWIR stack, and the contact layers, respectively.

The sample was grown on semi-insulating GaAs (100) by molecular beam epitaxy using As_2 as the arsenic species. After the growth of the bottom contact at 600 °C, the substrate temperature was lowered to 520 °C for the growth of the 20 periods MWIR stack. Growth interruption was performed before the growth of the middle contact to adjust the aluminum source temperature for the $Al_{0.27}Ga_{0.73}As$ barrier in the LWIR stack. At this point the substrate temperature was raised to 600 °C where it remained for the rest of the growth. Asymmetric X-ray scan measurement showed very little in-plane lattice relaxation with less than 186 part per million in-plane lattice constant increase. The low dark current and the good uniformity of the device also show that the device is of high quality despite of the high indium concentration.

The sample was processed into three different test structures for the characterization of the MWIR stack, LWIR stack, and the LWIR-MWIR stacks in series. The mesa areas of the test structures are all 200×200 μm^2 using standard photolithography wet chemical etching. The mesa structures of the LWIR-stack and the MWIR-LWIR-stack in series were formed by etching down from the top contact layer to the middle contact layer and to the bottom contact layer, respectively. The mesa structure of the MWIR-stack was formed first by completely removing the top contact layer and the LWIR stack, and then etching down from the middle contact layer to the bottom contact layer. A square ohmic contact ring composed of AuGe/Ni/Au was deposited on the periphery of the mesa and then alloyed for the ohmic contacts. Devices that used for 45° light coupling are polished on the substrate with a 45° facet, while no angle lapping and no grating were used on the devices for normal incidence illumination. Also, no substrate thinning was made on either set of devices.

5.3 Results and Discussion

In the dark current and photocurrent measurements, the substrate contact was grounded while positive or negative bias was applied to the top contact of the devices. Figure 5.2 shows the dark current for the MWIR stack measured at 77 K, 122 K, and 140 K, along with the 300 K window current measured at 30 K with a field of view (FOV) 180°. The sample is highly uniform and has very low dark current. The BLIP temperature was found to be 125 K up to ± 2 V and 120 K up to ± 3 V. The dark current measured at 35 K, 66 K and 77 K, along with the 300 K window current for the LWIR stack are shown in Fig. 5.3. The BLIP temperature is around 70 K for bias up to ± 2 V with a cutoff wavelength at 10 μm. 77 K operation could be achieved by shifting the cutoff wavelength to 9 μm. The 300 K window current was also calculated using the integration of the measured responsivity times the 300 K blackbody radiation spectrum with a 180° FOV [63]. The calculated results at 2V are 3.95×10^{-5} A/cm^2 and 1.93×10^{-3} A/cm^2 for the MWIR and LWIR stacks, respectively, which are in excellent agreement with the measured values at 2 V bias, as shown in Figs. 5.2 and 5.3 for the window currents.

The photocurrent spectra of the MWIR stack and LWIR stack were measured by using a 0.25 m grating monochromator and a calibrated blackbody source (T = 1000 °C). Smaller than 10 % variation of the device responsivity with temperature was observed from 30 K to 77 K. Figure 5.4 shows the peak responsivity versus bias for the MWIR stack measured at 77 K. The responsivity increases linearly with bias up to +3 V and -4 V, and then decreases. The responsivity spectra at 2 V and 3 V are given in Fig. 5.5 for the MWIR stack. The peak wavelength is at 4.3 μm with a maximum responsivity of 0.65 A/W at 3 V with 45° incidence. At this bias, the cut-on FWHM is at 3.9 μm and cut-off FWHM at 4.7 μm with a spectral width of 0.8 μm. The BLIP temperature for this MWIR stack is about 120 K at 3 V, and the BLIP spectral detectivity was found to be D^*_{BLIP} = 1.4×10^{11} cm-Hz$^{1/2}$/W at 77 K assuming a 10 % quantum efficiency. Besides relatively large doping in the well, the enhanced responsivity in the MWIR-stack is also related to the use of 35 % of indium in the InGaAs quantum well. The compressive strain induced in the $In_{0.35}Ga_{0.65}As$ quantum well leads to a 20 % reduction of the electron effective mass compared to no indium case. As a result, the intersubband absorption and hence the photoresponse are expected to increase over the unstrained case with the same well width. Figure 5.6 shows the peak responsivity at 9.4 μm versus bias voltage for the LWIR stack measured at 77 K. The responsivity increases linearly with bias up to ± 2 V and becomes saturated with a maximum value of 0.55 A/W at 2 V with 45° incidence. Figure 5.7 shows the spectral responsivity for the LWIR stack measured at 77 K and 2 V. The cut-on FWHM is at 8.6 μm, and cut-off FWHM is at 10 μm with a spectral width of 1.4 μm. The

LWIR stack is about 70 K BLIP at 2 V and the corresponding BLIP spectral detectivity of $D^{*}_{BLIP} = 1.8\times10^{10}$ cm-Hz$^{1/2}$/W was obtained assuming a 13 % quantum efficiency.

Responsivity of normal incidence without grating coupling was also measured for both of the MWIR and LWIR stacks. The results are shown in the corresponding figures (Figs. 5.4, 5.5, 5.6, and 5.7) along with the results of the 45° incidence. The responsivity ratio of the normal incidence to the 45° incidence is 40 % to 50 % and 35 % to 45 % for the MWIR and LWIR stack, respectively. According to quantum mechanical selection rule, the normal incidence absorption is not allowed in *n*-type QWIP. However, consistent experimental evidences [6, 20] have shown significant photoresponsivity with normal incidence without grating. Different explanations have been given [6, 68], but no concrete conclusions can be drawn at present stage.

The test structure of the MWIR-LWIR stacks in series were also measured with dark current dominated by the MWIR stack. The MWIR stack photoresponse was obtained and no LWIR photoresponse was observed even at very large bias. This could be due to the very high impedance in the MWIR stack caused by the very deep well using 35 % indium concentration. This will not affect the device performance when the signals of the two stacks have been integrated simultaneously. The wavelength tunability [62, 69] of this device by changing the bias voltage is still under study.

5.4 Conclusions

In conclusion, a high-strain two-stack, two-color QWIP has been demonstrated with very high performance. The device has 35 % of indium in the QW of the MWIR stack which produces high in-plane compressive strain. This strain enhances the responsivity of the MWIR stack while allowing the detection spectrum to cover the point of interest in the MWIR region. The detection peak wavelengths are at 4.3 μm and 9.6 μm and the corresponding maximum responsivities are 0.65 A/W and 0.55 A/W for the MWIR and

LWIR stacks, respectively, with 45° light incidence. Normal incidence without grating coupling also achieved responsivity of 0.25 A/W for either one stack from Figs. 5.4 and 5.6. Using grating coupling and substrate thinning will further enhance the device performance and make the present device a very practical infrared detector for the 2-color focal plane array IR imaging applications.

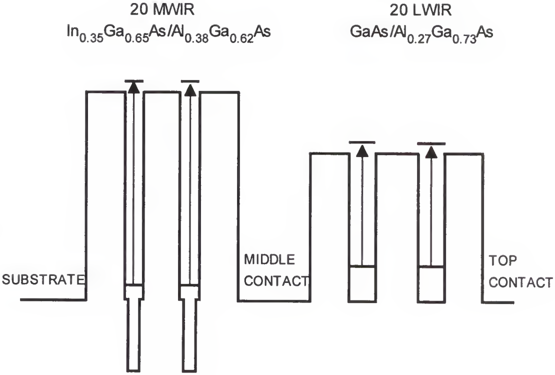
20 MWIR
$In_{0.35}Ga_{0.65}As/Al_{0.38}Ga_{0.62}As$
20 LWIR
$GaAs/Al_{0.27}Ga_{0.73}As$
SUBSTRATE
MIDDLE CONTACT
TOP CONTACT

Figure 5.1. The schematic conduction band diagram of the 2-stack, 2-color InGaAs/AlGaAs MWIR and AlGaAs/GaAs LWIR QWIP.

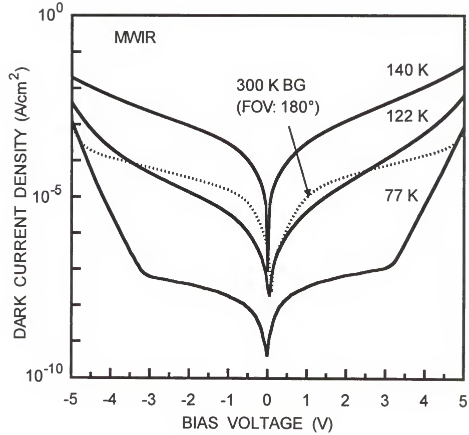

Figure 5.2. The dark I-V curves for the MWIR stack measured at 77K, 122K, and 140K, along with the 300K window current measured at 30K with a field of view (FOV) 180°.

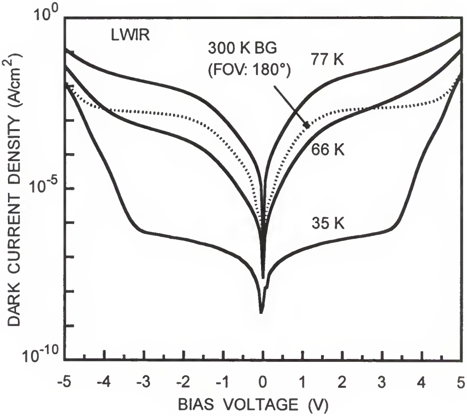

Figure 5.3. The dark I-V curves for the LWIR stack measured at 35K, 66K, and 77K, along with the 300K window current measured at 30K with a field of view (FOV) 180°.

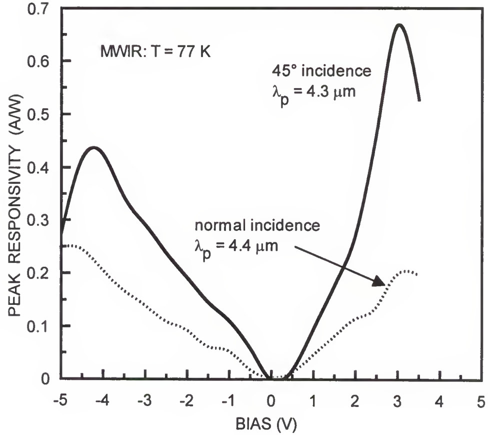

Figure 5.4. The peak responsivity versus bias for the MWIR stack measured at 77K at 45° incidence (solid line) and normal incidence without grating (dash line).

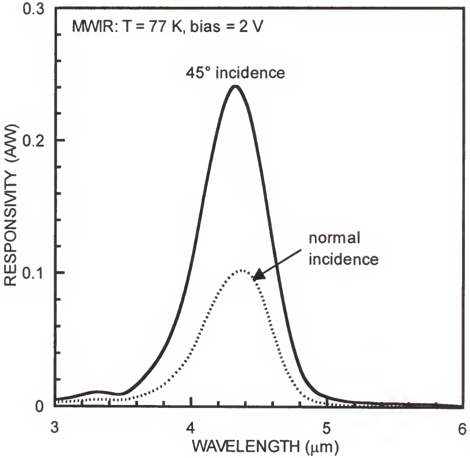

Figure 5.5. The responsivity spectra measured at 2V and 3V for the MWIR stack at 45° incidence (solid line) and 2V at normal incidence without grating (dash line).

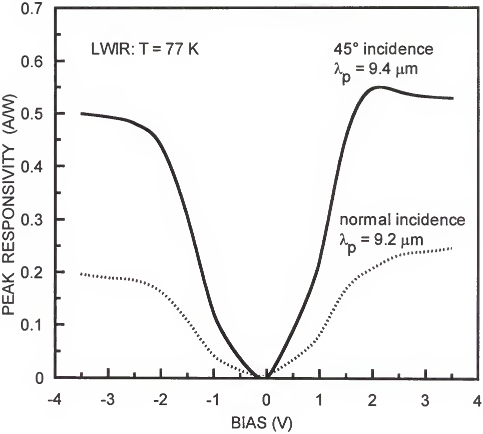

Figure 5.6. The peak responsivity at versus bias for the LWIR stack measured at 77K at 45° incidence (solid line) and normal incidence without grating (dash line).

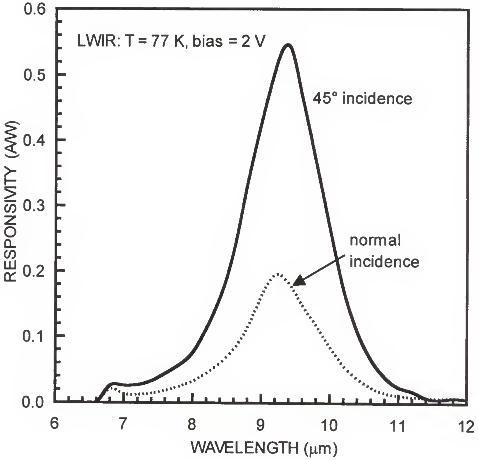

Figure 5.7. The responsivity spectra measured at 2V and 3V for the LWIR stack at 45° incidence (solid line) and 2V at normal incidence without grating (dash line).

CHAPTER 6
A TWO-STACK INDIRECT-BARRIER/TRIPLE-COUPLED QUANTUM WELL INFRARED PHOTODETECTOR

6.1 Introduction

In the atmospheric transmission window for infrared radiation, the 3 – 5 μm mid-wavelength infrared (MWIR) and 8 – 14 μm long-wavelength infrared (LWIR) spectral regions are of particular importance to a wide variety of technological specialties, such as remote astronomical telescope, seeker-tracker system, ultra-low loss communication system, and space-borne surveillance radar. For the MWIR detection, high performance InAlAs/InGaAs quantum well infrared photodetectors (QWIPs) grown on InP substrate have been developed [33, 70, 71]. But they are not suitable to integrate with the LWIR QWIPs which were usually grown on GaAs substrate. Monolithically integrated Schottky barrier PtSi staring FPA has been developed for MWIR imaging applications, while for LWIR HgCdTe hybrid staring FPAs are widely used. However, HgCdTe has the most serious technological problems of any semiconductor material in mass production. Si-based optoelectronic devices have also attracted great interest because of the potential for monolithic integration and the well-developed processing technology. SiGe/Si QWIPs have rapidly developed in recent years [72-74] which shown a compatible LWIR photoresponse to the conventional GaAs/AlGaAs LWIR QWIPs, but the MWIR photoresponse is still about one order of magnitude lower than that of III-V MWIR QWIPs.

Due to the mature GaAs growth technologies and the ability of integration with Si-based signal-processing electronics, integration of GaAs-based MWIR and LWIR QWIPs [13-20] has of particular interest to the engineers. We have developed and characterized two MWIR/LWIR-stacked QWIPs and one voltage-tunable multicolor triple-coupled QWIP as described in the previous chapters. The high performance of these QWIPs give us a motivation to do more studies. In this chapter, We demonstrated a two-stack indirect-barrier/triple-coupled quantum well infrared photodetector for mid- and long-wavelength detection and studied the effects of doping density and the number of the QW periods on the performance of these devices.

6.2 Device Growth and Fabrications

The basic device structure for the multicolor 2-stack IB/TC-QWIP is an indirect-barrier QWIP consisting of a 50 nm undoped $Al_{0.55}Ga_{0.45}As$ barrier and a 3 nm heavily doped GaAs QW for the MWIR detection and an $In_{0.05}Ga_{0.95}As/GaAs/Al_{0.19}Ga_{0.81}As$ triple-coupled QWIP for LWIR detection. The MWIR IB-QWIP is designed to have a detection peak at 4.3 μm while the LWIR TC-QWIP has multiple response peaks that are voltage-tunable in the 8 – 12 μm LWIR band. To study the effects of doping density and the number of the QW periods on the performance of these devices, four QWIP samples (N301 to N304) with different layer structures, doping density and the number of the QW periods, have been grown on semi-insulating GaAs (100) substrate by molecular beam epitaxy (MBE). Table 6.1 shows the layer structure of the two-stack IB/TC-QWIP with two different doping densities, $N_d = 5\times10^{17}$ cm^{-3} and 1×10^{18} cm^{-3}, and two different numbers of QW periods (20 and 40 periods). The schematic diagram of the conduction band of this QWIP is shown in Figs. 6.1(a) and 6.1(c). The transition schemes for the LWIR TC-QWIP have been described in chapter 4 except the tunable wavelength range is designed to be of 9 – 10 μm. The transition schemes for the MWIR IB-QWIP is indicated by the numbers in Fig. 6.1(c). The photon-excited electron is generated from E_0^Γ to E_1^Γ where it will escape out of the well and begin to transport above the Γ barrier (No. 2). Then it will be rapidly scattered into the X valley (No. 3) and transported towards the

GaAs QW (No. 4). There are two transport mechanisms which should be considered in the GaAs QW region. One is the capture mechanism and the other is the tunneling mechanism (No. 5). The latter will contribute to the photocurrent while the former not. It is shown [75] that the tunneling time τ_t^X is much shorter than the recapture time $\tau_c^{X\Gamma}$. Hence, the tunneling mechanism is dominated in this region. Due to the mix Γ-X coupling effects, the photoexcited electrons can be efficiently collected as photocurrent. The transmission probability calculated from the transfer matrix method (TMM) is shown in Figs. 6.1(b) and 6.1(d) for LWIR-stack and MWIR-stack, respectively. The peak wavelengths of $E_1 \rightarrow E_3$ transition for the LWIR-stack and $E_1 \rightarrow E_C$ transition for the MWIR-stack were found to be 10.7 μm and 4.3 μm, respectively, which are in good agreement with the measured peaks, 10.9 μm and 4.3 μm, respectively.

6.3 Results and Discussion

The test devices with an active area of 200×200 μm^2 mesa structure were fabricated on these QWIP samples using standard wet chemical etching for device characterization use. The mesa structure of the MWIR-stack was formed first by completely removing the top contact layer and the LWIR-stack, and then by etching down from the middle contact layer to the bottom contact layer. The mesa structures of the LWIR-stack and stacked-QWIP were formed by etching down from the top contact layer and stopping at the middle and bottom contact layers, respectively. A square ohmic contact ring composed of AuGe/Ni/Au was then deposited on the periphery of the mesa structure of the highly doped GaAs contact layer and alloyed for ohmic contacts. Finally, the devices were prepared with a 45° polished facet on the substrate for coupling incident IR radiation into the multiquantum wells. To study the performance dependence of the QWIP on the doping density and the number of the QW periods, the dark current versus bias voltage and the spectral responsivity measurements have been performed on these devices. The photocurrent spectra were measured with 45° facet illumination using a 0.25 m grating monochromator and a calibrated blackbody source $T = 1000$ °C.

6.3.1 LWIR TC-QWIPs

6.3.1.1 Effects of doping density

Figures 6.2(a) and 6.2(b) show the dark current density versus bias voltage ($J - V$) curves for the 20-period TC-QWIPs with doping densities of 5×10^{17} and 1×10^{18} cm^{-3}, respectively. The higher doping density in the QW shows a higher dark current which is in agreement with the thermionic emission model, Eq. (2.31), i.e. the dark current is proportional to the thermal-generated electron density under the same electric field condition. The BLIP temperature for these devices was found to be 60 K for $V_b < 6$ V and 77 K for $V_b < 2$ V for the low doped device. Figures 6.3(a) and 6.3(b) show the dark current density versus bias voltage ($J - V$) curves for the 40-period TC-QWIPs with doping densities of 5×10^{17} and 1×10^{18} cm^{-3}, respectively. The results show a similar behavior with the 20-period devices.

The responsivity versus wavelength, measured at $V_b = 5$, 6, 7, and -5 V and $T = 60$ K, for the 20-period TC-QWIPs with two different doping densities are shown in Figs. 6.4(a) and 6.4(b) respectively; the insets show the linear dependence of the peak wavelength with applied bias voltage. Two main transition schemes, $E_1 \rightarrow E_C$ and $E_1 \rightarrow E_3$, have been observed in both devices. Higher doping device has a higher responsivity for the $E_1 \rightarrow E_C$ transition. On the contrary, higher doping device has a lower responsivity for the $E_1 \rightarrow E_3$ transition. It is indicated that there are different carrier transport mechanisms associated with these two transitions. More detailed analysis should be surveyed. The voltage tunabilities for both devices are ranging from 9 to 10.7 μm in the LWIR band. Figures 6.5(a) and 6.5(b) show the responsivity versus wavelength, measured at $V_b = 10$, 12, 14, and -10 V and $T = 60$ K, for the 40-period TC-QWIPs with two different doping densities, respectively; the insets show the linear dependence of the peak wavelength with applied bias voltage. The results show a similar behavior with the 20-period devices.

6.3.1.2 Effects of the QW periods

It is interesting to note that increasing the QW periods does not show any improvement or beneficial effect in spectral responsivity of the QWIP; the device with 40-period QWs requires two times of bias voltage to produce the same responsivity as the 20 periods device.

6.3.2 MWIR IB-QWIPs

Figures 6.6 and 6.7 show the temperature dependence of the dark *J-V* for the 20-period (N301 and N303) and 40-period (N302 and N304) MWIR-stacks, respectively. The higher doping density in the QW shows a higher dark current which is in agreement with the thermionic emission model. The dark currents are several orders of magnitude larger than expected even on the basis of an indirect thermionic emission barrier height of 178 meV. The 300 K window currents with a 180° FOV are also shown in Figs. 6.6 and 6.7 and the BLIP temperature is found to be 40 K for all four devices.

Figures 6.8(a) and 6.8(b) show the responsivity spectra of the 20-period MWIR-stack devices with doping densities of 5×10^{17} and 1×10^{18} cm^{-3}, respectively. The detection peak wavelengths were found to be of 4.3 μm and were independent of bias voltage and the doping density. The peak responsivities were found to be increased linearly with the bias voltage and the doping density, and both devices showed the PV response.

Figures 6.9(a) and 6.9(b) show the responsivity spectra of the 40-period MWIR-stack devices with doping densities of 5×10^{17} and 1×10^{18} cm^{-3}, respectively. The detection peak wavelengths were found to be of 4.3 μm and were independent of bias voltage and the doping density. The peak responsivities were found to be increased linearly with the bias voltage and the doping density. Figure 6.10 shows the PV response for both devices.

The peak responsivity and the peak detectivity were found to be of 0.047 A/W, 1×10^{12} cm-Hz$^{1/2}$/W and 0.02 A/W, 6.3×10^{11} cm-Hz$^{1/2}$/W at 0 V for the 40-period MWIR-stack devices, respectively. This large D^* is comparable to the MWIR-stack using the direct gap material InGaAs/InAlAs grown on the InP substrate.

The performance dependence of the MWIR-stacks on the doping density and the number of the MQW periods has been studied. The results showed that the higher doping density in the QW, the higher dark current, the responsivity, and the D^* of the PV mode will be generated for the doping range from 5×10^{17} cm^{-3} to 1×10^{18} cm^{-3}.

6.3.3 Stacked IB/TC-QWIPs

6.3.3.1 20-period Stacked IB/TC-QWIPs

Figures 6.11(a) and 6.11(b) show the dark *J-V* curves measured at 77, 58, and 44 K for the 20-period (N301 and N303) two-stack IB/TC-QWIPs with $N_d = 5\times10^{17}$ and 1×10^{18} cm^{-3}, respectively. The results show that device (N303) with higher doping density in the QW has a higher dark current than the lower doped device (N301). The 300 K window currents with a 180° FOV for both devices are also included in Fig. 6.11, and the BLIP temperatures were found to be 35 K and 40 K for N301 and N303, respectively. Due to the higher than expected dark current in the MWIR-QWIP, the BLIP temperatures of the two-stack IB/TC-QWIPs are limited by the MWIR IB-QWIPs.

Figures 6.12(a) and 6.12(b) show the responsivity versus wavelength for the 20-period MWIR and LWIR stacked-QWIPs (N301 and N303), respectively, measured at $T = 40$ K. The detection peak wavelength was found to be at 4.3 μm for both devices. The responsivitiy was found to increase with increasing doping density and bias voltage. Both photoconductive (PC) and photovoltaic (PV) responses were observed for these IB-QWIPs. The peak responsity was found to be of 23 mA/W and 30 mA/W at 0 V for N301 and N303 devices, respectively. For LWIR TC-QWIP stack, two main response peaks were observed: one is the voltage-tunable $E_1 \rightarrow E_3$ transition under positive bias voltages (quantum confined Stark shift effect) and the other is the $E_1 \rightarrow E_C$ transition under negative bias voltages. The tunable peak wavelengths were found to be from 10.2 to 9.6 μm and 10 to 9.4 μm for N301 and N303 devices, respectively, with responsivity increasing with increased bias voltage. Figures 6.13(a) and 6.13(b) show the bias dependence of the peak responsivity for the 20-period stacked-QWIPs. It is noted that only MWIR response was observed for $-5\ \text{V} < V_b < 7\ \text{V}$. The maximum peak responsivities in this regime were found to be 0.13 A/W and 0.21 A/W for N301 and N303 devices, respectively, at $V_b = 4$ V. Both the MWIR and LWIR detection peaks appear outside this bias range. Therefore, using the two-stack QWIP reported here it is possible to simultaneously detect both the MWIR and LWIR bands at $V_b \geq 7$ V or $V_b \leq$ -5V. In addition, it is also possible to use this two-stack IB/TC-QWIP as a voltage-tunable two-color or multi-color QWIP for the MWIR and LWIR dual band detection.

6.3.3.2 40-period Stacked IB/TC-QWIPs

Figures 6.14(a) and 6.14(b) show the dark *J-V* curves for the 40-period (N302 and N304) two-stack IB/TC-QWIPs with $N_d = 5\times10^{17}$ and 1×10^{18} cm^{-3}, respectively. The 300 K window currents with a 180° FOV are also included in Fig. 14, and the BLIP temperatures were found to be 45 K and 35 K for N302 and N304, respectively.

Figures 6.15(a) and 5.15(b) show the responsivity versus wavelength for the 40-period stacked-QWIPs (N302 and N304), respectively, measured at T = 40 K and different bias voltages. The detection peak wavelength was found to be at 4.3 μm for the MWIR stack, and was independent of the bias voltage and doping density. Contrary to the 20-period stacked-QWIPs, no PV response was observed in both devices. For the LWIR stack, two to three detection peaks due to $E_1 \rightarrow E_3$ and $E_1 \rightarrow E_C$ transitions under positive and negative bias voltages were found in the LWIR TC-QWIPs. The peak detection wavelengths were found to be voltage tunable (Stark shift) from 9.8 to 9.25 μm and from 10.2 to 9.7 μm for N302 and N304 devices, respectively, with increasing bias voltage.

Figures 6.16(a) and 6.16(b) show the bias dependence of the peak responsivity of the 40-period stacked-QWIPs. The MWIR peak responsivities were found to increase with increasing bias voltage for N302, while for N304, the peak responsivity was first increased with the applied bias voltage and it then decreased with increasing bias voltage for $-8\ \text{V} < V_b < 6\ \text{V}$.

6.4 Conclusions

Characterizations of the four sets of the two-stack IB/TC-QWIPs, with two different doping densities ($N_d = 5\times10^{17}\ \text{cm}^{-3}$ and $1\times10^{18}\ \text{cm}^{-3}$) and two different numbers of the QW periods (20 and 40 periods), have been performed to study their effects on the performance of these devices. The responsivity of the MWIR IB-QWIPs was found to increase with increasing doping density, while for LWIR TC-QWIPs the responsivity was found to be nearly independent of the doping density. Study of the effect of the number of QW periods revealed that the responsivity of the 20-period stacked-QWIPs is better than those of the 40-period stacked-QWIPs. The two-stack IB/TC-QWIPs reported here maybe used to detect simultaneously two colors in the MWIR and LWIR bands at the same bias voltage (see Figs.6.14 and 6.16). It can also be used as a voltage tunable (PV and PC mode operation) two- or three-color QWIP for the MWIR and LWIR dual-band detection. Strong quantum confined Stark effect (QCSE) due to ($E_1 \rightarrow E_3$) transition was observed in the TC-QWIPs, enabling the peak detection wavelength to be tuned by the applied bias voltage in the 8 – 12 μm LWIR band. Optimization of device parameters in the two-stack IB/TC-QWIPs should further improve the performance of this stacked QWIP for the MWIR and LWIR dual-band detection.

Table 6.1. Layer structures of the 2-color 2-stack IB/TC QWIP.

Layer		**Thickness (Å)**	**Dopant**	**Concentration (cm^{-3})**
n^+ GaAs (top contact)		3000	Si	2×10^{18}
i $Al_{0.21}Ga_{0.79}As$		500	---	---
n $In_{0.05}Ga_{0.95}As$	# period (LWIR)	72	Si	QW-doping
i $Al_{0.21}Ga_{0.79}As$		11	---	---
i GaAs		40	---	---
i $Al_{0.21}Ga_{0.79}As$		11	---	---
i GaAs		40	---	---
i $Al_{0.21}Ga_{0.79}As$		500	---	---
n^+ GaAs (middle contact)		5000	Si	2×10^{18}
i $Al_{0.55}Ga_{0.45}As$		500	---	---
n GaAs	# period (MWIR)	30	Si	QW-doping
i $Al_{0.55}Ga_{0.45}As$		500	---	---
n^+ GaAs (bottom contact)		5000	Si	2×10^{18}
S.I. GaAs substrate		635 +/- 25 μm	---	---

Note: # Period and QW-doping

Part #	# Period	QW-doping (cm^{-3})
N301	20	5×10^{17}
N302	40	5×10^{17}
N303	20	1×10^{18}
N304	40	1×10^{18}

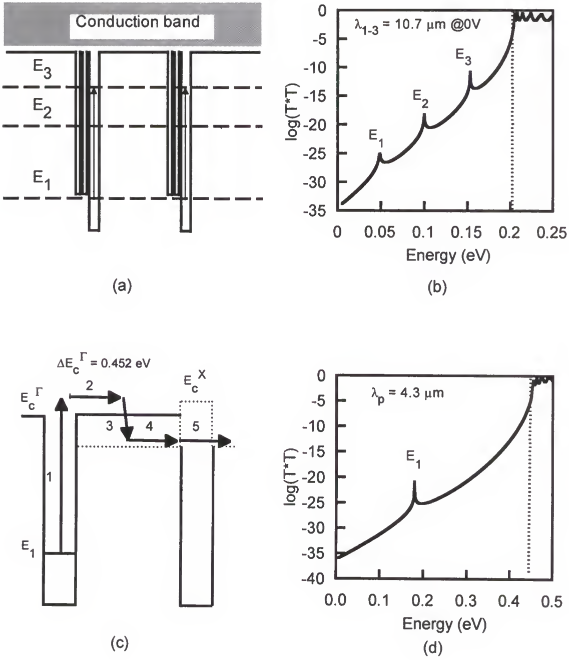

(a) (b) (c) (d)

Figure 6.1. The schematic conduction band diagrams, (a) and (c), and the transmission probabilities, (b) and (d) of the two-stack IB/TC QWIP.

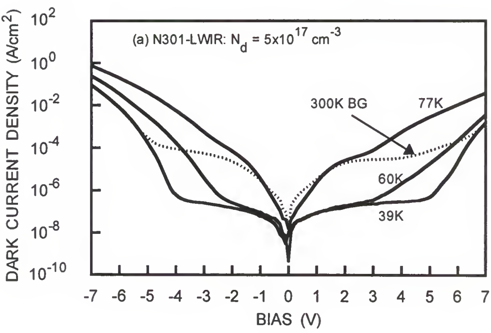

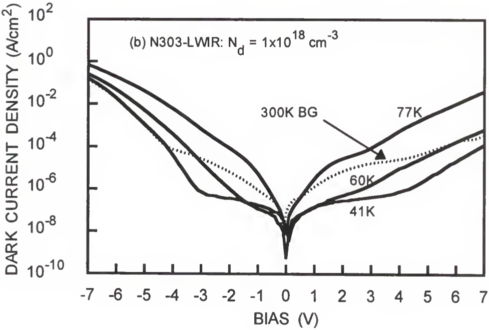

Figure 6.2. Dependence of the dark *J-V* for the 20-period LWIR-stack on doping density, (a) 5×10^{17} and (b) 1×10^{18} cm^{-3}.

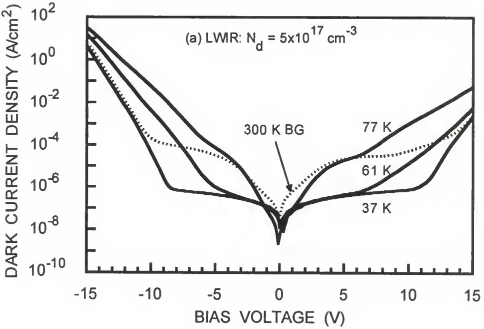

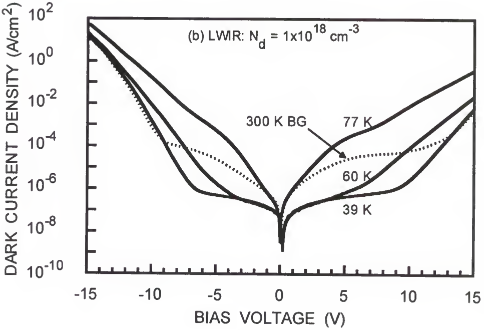

Figure 6.3. Dependence of the dark *J-V* for the 40-period LWIR-stack on doping density, (a) $5\text{x}10^{17}$ and (b) $1\text{x}10^{18}$ cm^{-3}.

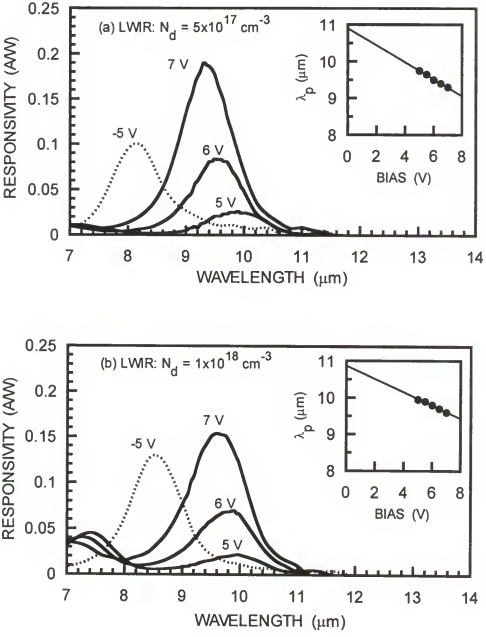

Figure 6.4. Dependence of the spectral responsivity for the 20-period LWIR-stack on doping density, (a) 5×10^{17} and (b) 1×10^{18} cm^{-3}.

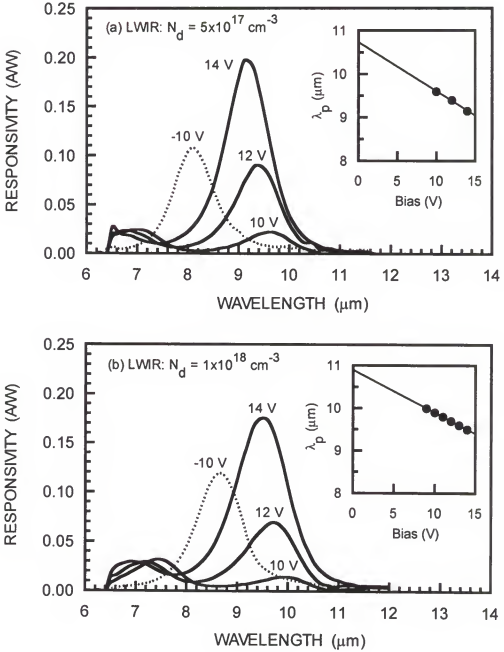

Figure 6.5. Dependence of the spectral responsivity for the 40-period LWIR-stack on doping density, (a) $5x10^{17}$ and (b) $1x10^{18}$ cm^{-3}.

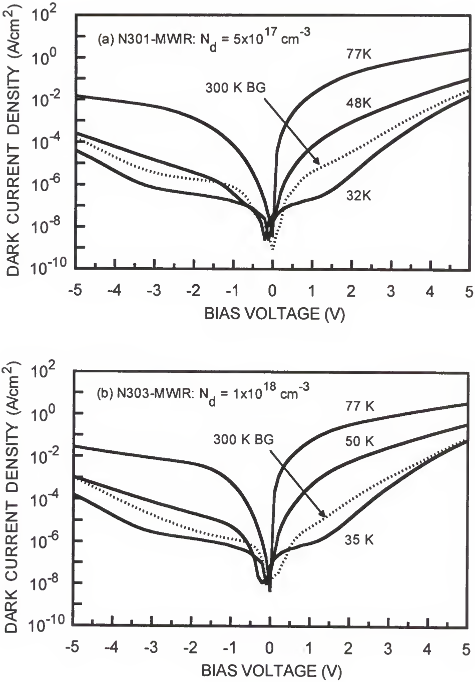

Figure 6.6. Dependence of the dark *J-V* for the 20-period MWIR-stack on doping density, (a) 5×10^{17} and (b) 1×10^{18} cm^{-3}.

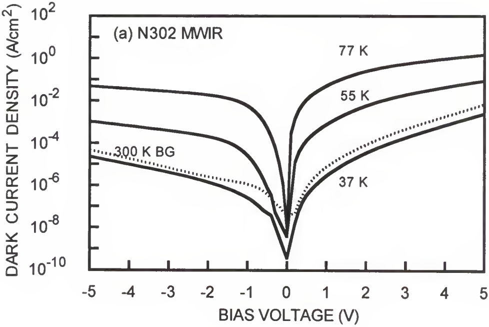

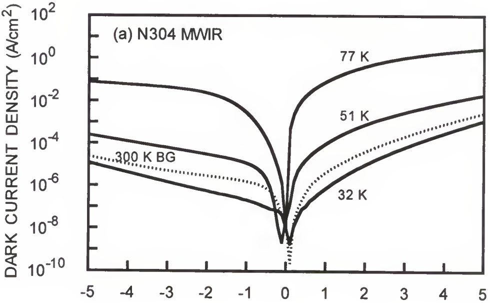

Figure 6.7. Dependence of the dark *J-V* for the 40-period MWIR-stack on doping density, (a) 5×10^{17} and (b) 1×10^{18} cm^{-3}.

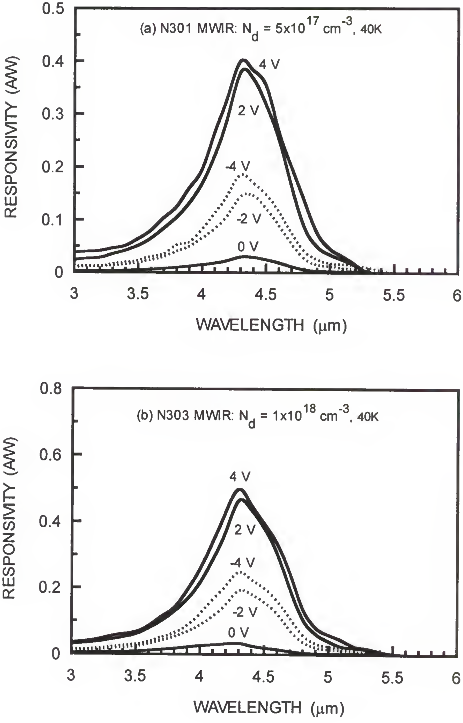

Figure 6.8. Dependence of the spectral responsivity for the 20-period MWIR-stack on doping density, (a) 5×10^{17} and (b) 1×10^{18} cm^{-3}.

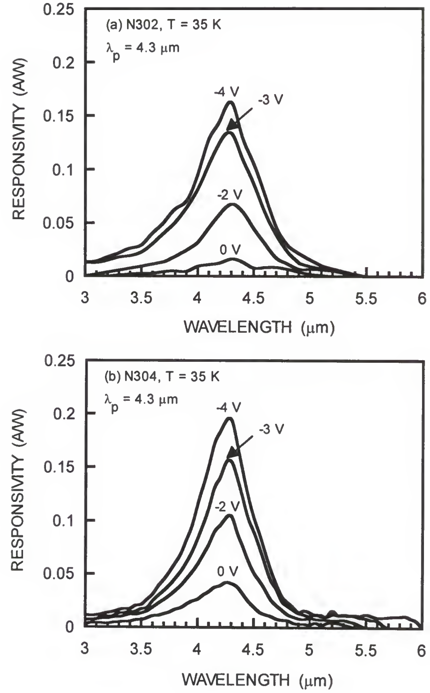

Figure 6.9. Dependence of the spectral responsivity for the 40-period MWIR-stack on doping density, (a) 5×10^{17} and (b) 1×10^{18} cm^{-3}.

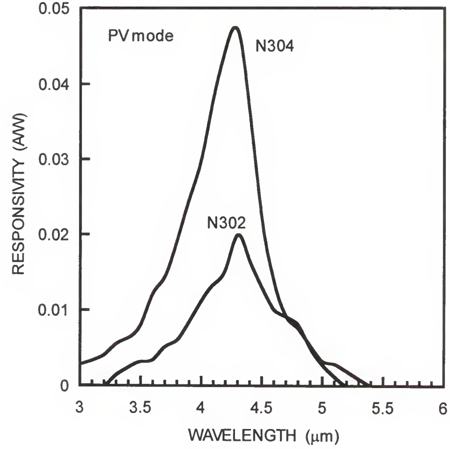

Figure 6.10. The PV spectral responsivity of the 40-period MWIR-stack.

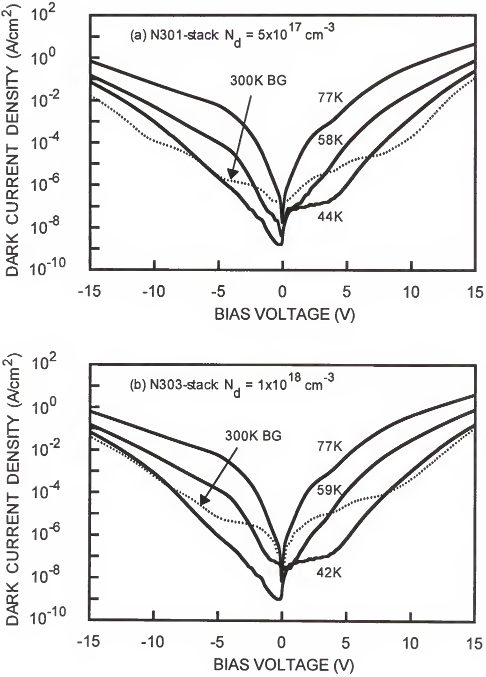

Figure 6.11. Dependence of the dark *J-V* for the 20-period stacked-QWIP on doping density, (a) $5\text{x}10^{17}$ and (b) $1\text{x}10^{18}$ cm^{-3}.

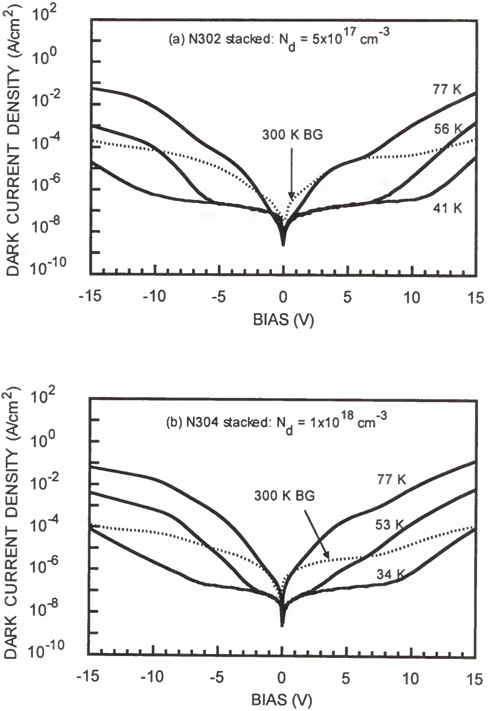

Figure 6.12. Dependence of the dark *J-V* for the 40-period stacked-QWIP on doping density, (a) 5×10^{17} and (b) 1×10^{18} cm^{-3}.

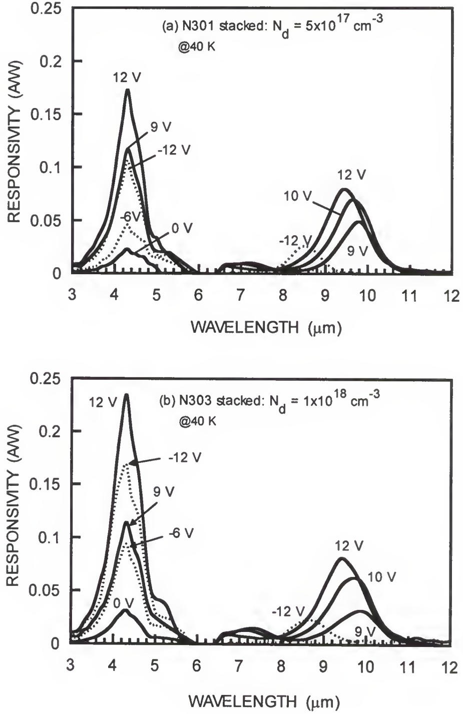

Figure 6.13. Dependence of the spectral responsivity for the 20-period stacked-QWIP on doping density, (a) $5x10^{17}$ and (b) $1x10^{18}$ cm^{-3}.

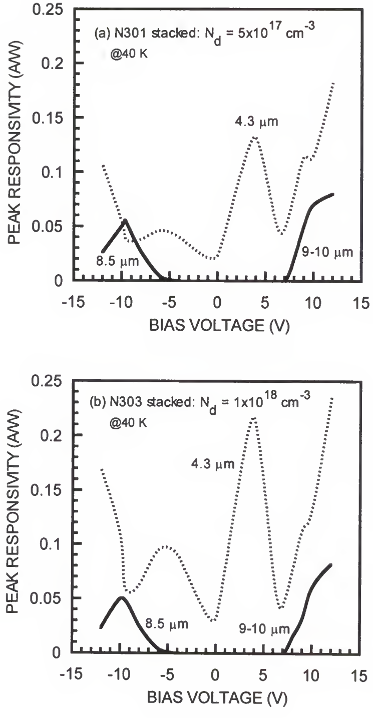

Figure 6.14. Bias dependence of the peak responsivity for the 20-period stacked-QWIP with different doping density, (a) $5x10^{17}$ and (b) $1x10^{18}$ cm^{-3}.

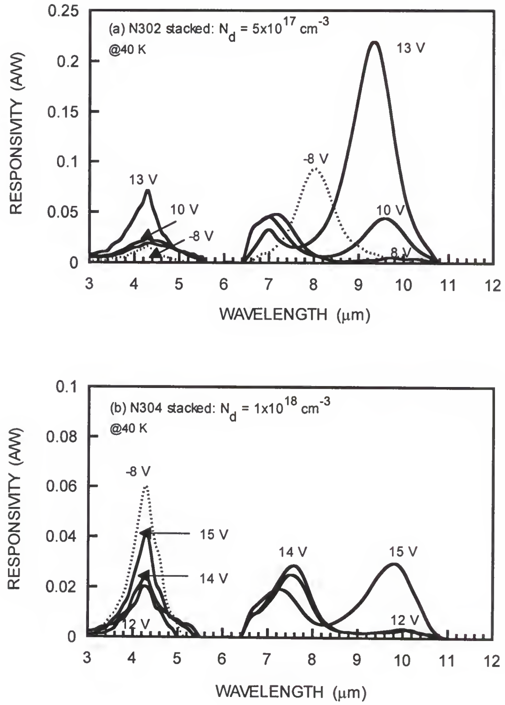

Figure 6.15. Dependence of the spectral responsivity for the 40-period stacked-QWIP on doping density, (a) 5×10^{17} and (b) 1×10^{18} cm^{-3}.

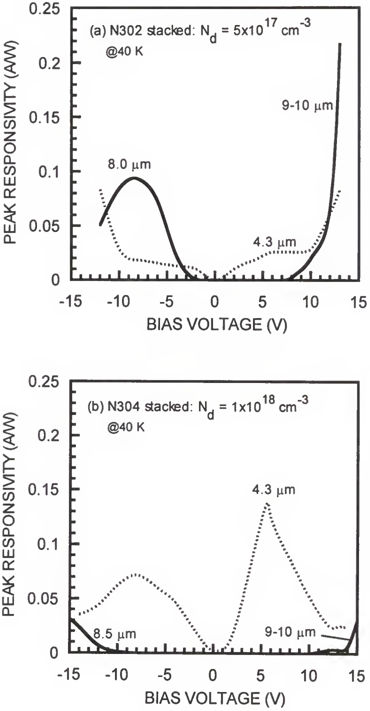

Figure 6.16. Bias dependence of the peak responsivity for the 40-period stacked-QWIP with different doping density, (a) 5×10^{17} and (b) 1×10^{18} cm^{-3}.

CHAPTER 7
A HIGH PERFORMANCE HIGH STRAIN TRIPLE-COUPLED QUANTUM WELL INFRARED DETECTOR

7.1 Introduction

Quantum well infrared photodetectors (QWIPs) based on high-strain InGaAs material grown on GaAs substrate [17, 37, 67, 68, 76] have been widely investigated in recent years for both 3 – 5 μm mid-wavelength and 8 – 14 μm long-wavelength infrared detection. Due to the quantum mechanical selection rule as described in chapter 2, the intersubband absorption under normal incident illumination is usually not allowed in *n*-type QWIPs. As a result, a metal or dielectric grating coupler [11, 48, 77] is required for most *n*-type QWIPs in order to achieve normal incident absorption. The unique feature of these high strain QWIPs is that a large normal incident absorption without a grating coupler has been observed, which has a responsivity ratio of the normal incidence to the 45° incidence ranging from 30 % to 50 %. It indicates that high sensitivity gratingless normal incidence *n*-type QWIPs can be achieved by optimizing the QWIP's structure. In addition, it can greatly reduce the fabricating complexity which can significantly lower the cost of *n*-type QWIP focal plane arrays (FPAs).

In chapter 4 we have demonstrated a new voltage-tunable multicolor lightly strained InGaAs/AlGaAs/GaAs triple-coupled quantum well infrared photodetector (TC-QWIP) for 7 – 14 μm detection. In addition, a high-strain InGaAs/GaAs/AlGaAs MWIR-QWIP depicted in chapter 5, also showed a large normal incident absorption. In this chapter a high sensitivity triple-coupled quantum infrared photodetector (TC-QWIP) using high-strain *n*-type $In_{0.25}Ga_{0.75}As/Al_{0.11}Ga_{0.89}As/In_{0.12}Ga_{0.88}As$ asymmetrical coupled quantum well structure has been developed for 8 – 14 μm LWIR detection.

7.2 Device Growth and Fabrications

Figure 7.1(a) shows the schematic diagram of the conduction band and the bound state energy levels for this high-strain TC-QWIP structure, and Fig. 7.1(b) shows the calculated transmission probability under zero bias condition. It consists of a highly doped ($n = 7\times10^{17}$ cm^{-3}) high-strain (HS) $In_{0.12}Ga_{0.88}As$ quantum well of 5.5 nm thick, two undoped thin $Al_{0.11}Ga_{0.89}As/In_{0.12}Ga_{0.88}As$ (2/4 nm layer thickness) quantum wells separated by a 50 nm $Al_{0.11}Ga_{0.89}As$ barrier layer; the structure is repeated 5 and 10 times in series to form a two-stack HS TC-QWIP with 5-period and 10-period multiquantum wells. Finally, a 0.1 µm thick undoped GaAs layers [78, 79] was grown between the multiquantum wells and the top and bottom GaAs contact layers (both doped to $n = 2\times10^{18}$ cm^{-3}) to reduce the tunneling current from contacts to QWs which results in a lower dark current.

For the TC-QWIP, due to the strong coupling effect of the three asymmetrical QWs and two thin AlGaAs barriers, the bound states in the $In_zGa_{1-z}As$ QWs and the first excited state in the $In_xGa_{1-x}As$ QW are coupled to form the second (E_2) and third (E_3) bound states inside the TC-QWs as illustrated in Fig. 7.1(a). The intersubband transition for this TC-QWIP is dominated by the $E_1 \rightarrow E_3$ ($\lambda_{13} = 10.9$ µm at 0 V) bound-to-bound (BTB) state transition, while a secondary photoresponse peak due to $E_1 \rightarrow E_C$ ($\lambda_{1C} = 8.8$ µm at 0 V) bound-to-continuum (BTC) state transition was also observed in this device.

The test structures with an active area of 200×200 µm^2 were fabricated on the QWIP samples by standard wet chemical etching for device characterization use. The mesa structure of the 5-period HS TC-QWIP was formed first by completely removing the top contact layer and the 10-period-stack, and then by etching down from the middle contact layer to the bottom contact layer. The mesa structure of the 10-period HS TC-QWIP was formed by etching down from the middle contact layer to the bottom contact layer. A square ohmic contact ring composed of AuGe/Ni/Au was then deposited on the periphery of the mesa structure of the highly doped contact layers and alloyed for the ohmic contacts. Finally, the devices were prepared both with 45° polished facet on the substrate for coupling incident IR radiation into the quantum wells and with a front-side normal incident illumination.

7.3 Results and Discussion

7.3.1 Dark Current Measurements

Figure 7.2 shows the temperature dependence of the dark *J-V* of the 5-period HS TC-QWIP. The dark *J-V* curves show an asymmetric behavior which is a common result for the *n*-type QWIPs. The 300 K window currents with a 180° FOV was also shown in Fig. 7.2, and the BLIP temperature was found to be 65 K with bias voltages up to -3 V. This is 5 K higher than the previous lightly strained TC-QWIP discussed in chapter 4. Figure 7.3 shows the temperature dependence of the dark *J-V* of the 10-period HS TC-QWIP. The dark *J-V* curves show a similar behavior as those of the 5-period HS TC-QWIP. The 300 K window currents with a 180° FOV was also shown in Fig. 7.3, and the BLIP temperature was found to be 65 K with biases up to -5 V, which is same as the 5-period QWIP. For comparison, Fig. 7.4 shows the dark *J-V* versus the electric field (assumed the bias voltage is uniformly distributed across the whole structure) for the 5- and 10-period TC- QWIPs at 77 K. The result shows that the 5-period device has a higher dark current than that of the 10-period QWIP under same applied electric field.

7.3.2 Photoresponse Measurements

The photocurrent spectra were measured with 45° facet illumination and with front-side normal incidence illumination using a 0.25 m grating monochromator and a calibrated blackbody source at $T = 1000°$ C. Figure 7.5 shows the spectral responsivity of the 5-period HS TC-QWIP measured with a 45° facet at V_b = -3, -2.8 and -2.6 V and T =

30 K; the inset shows the linear dependence of the peak wavelengths for both $E_1 \rightarrow E_3$ and $E_1 \rightarrow E_C$ transitions with the applied bias voltage. The wavelength tunabilities for this device are ranging from 6.9 to 7.3 μm and 9.6 to 10.1 μm for the $E_1 \rightarrow E_C$ and $E_1 \rightarrow E_3$ transitions, respectively. The interpolated peak wavelengths at zero bias are found to be 8.6 μm and 11.1 μm for the $E_1 \rightarrow E_C$ and $E_1 \rightarrow E_3$ transitions, respectively, which are in good agreement with calculated peak wavelengths at zero bias: 8.8 μm and 10.9 μm, respectively, as shown in Fig. 7.1(b). The peak responsivities were found to be increased with the bias voltage up to -3 V and the maximum peak responsivity was found to be of 2.77 A/W at λ_p = 9.6 μm, V_b = -3 V and T = 30 K. We also measured the spectral responsivity of this device with a front-side normal incidence illumination. The results are shown in Fig. 7.6 along with those of 45° facet illumination. It is found that the responsivity ratios of the normal incidence to the 45° incidence are 55 % - 75 % and 60 % - 80 % for the $E_1 \rightarrow E_C$ and $E_1 \rightarrow E_3$ transitions, respectively. Figure 7.7 shows the spectral responsivity of the 10-period HS TC-QWIP measured with a 45° facet illumination at V_b = -5, -4.5 and -4 V and T = 30 K; the inset shows the linear dependence of the peak wavelengths for both $E_1 \rightarrow E_3$ and $E_1 \rightarrow E_C$ transitions with the applied bias voltage. The wavelength tunabilities and the peak responsivities for this device are found to be almost the same as those of 5-period device, but reqires a higher bias voltage applied to the device. Figure 7.8 shows the peak responsivities versus the bias voltage for both the normal incidence and 45° incidence devices measured at T = 30 K. It is found that the responsivity ratios of the normal incidence to the 45° incidence are 30 % - 40 % and 50 % - 60 % for the $E_1 \rightarrow E_C$ and $E_1 \rightarrow E_3$ transitions, respectively, which are lower than those of the 5-period device. Figure 7.9 shows the temperature dependence of the peak responsivity for the $E_1 \rightarrow E_3$ transition versus the electric field with a 45° incidence illumination. From the results of this study, it is found that (1) the 5-period device has larger peak responsivity than those of the 10-period device under the same temperature and electric field conditions and (2) for each same period device, the peak responsivity is

increased by up to 200 % when the temperature was increased from 30 K to 77 K, and (3) both devices show very large normal incidence absorption.

7.3.3 Detectivity

Figures 7.10 and 7.11 show the calculated detectivities for both 5-period and 10-period devices at 77 K and BLIP temperature 65 K, respectively, using the noise model [66] by Wang et al. The results show that the 10-period device has a higher non-BLIP detectivity of 2.93×10^{10} cm-Hz$^{1/2}$/W at $\lambda_p = 9.8$ μm, $V_b = -4.5$ V and 77 K, but the 5-period device has a higher BLIP detectivity of 4.41×10^{10} cm-Hz$^{1/2}$/W at $\lambda_p = 9.6$ μm, $V_b = -3$ V and 65 K.

7.4 Conclusions

In conclusion, we have demonstrated a very high performance voltage-tunable TC-QWIP using high-strain *n*-type $In_{0.25}Ga_{0.75}As/Al_{0.11}Ga_{0.89}As/In_{0.12}Ga_{0.88}As$ asymmetrical coupled quantum well structure for 8 – 14 μm LWIR detection. The maximum responsivities at $\lambda_p = 9.6$ μm were found to be 1.71 A/W and 2.77 A/W at $V_b = -2.8$ V, -3 V and $T = 77$ K, 30 K, respectively, for the 5-period device. For the 10-period device, the maximum responsivities were found to be 1.3 A/W and 2.71 A/W at $\lambda_p = 9.8$ μm, $V_b = -4.5$ V, and $T = 77$ K, and at $\lambda_p = 9.6$ μm, $V_b = -5$ V, and $T = 30$ K, respectively. The maximum detectivities were found to be 1.44×10^{10} cm-Hz$^{1/2}$/W and 2.93×10^{10} cm-Hz$^{1/2}$/W at $\lambda_p = 9.9$ μm, $V_b = -2.6$ V and $T = 77$ K, and at $\lambda_p = 9.8$ μm, $V_b = -4.5$ V, and $T = 77$ K for the 5-period and 10-period devices, respectively. It is shown that this HS TC-QWIP can be used as a voltage-tunable two-color or multicolor QWIP for lower background LWIR detection. In addition, the device shows very large normal incidence absorption, which offers the excellent possibility for fabricating low cost, large area gratingless TC-QWIP focal plane arrays (FPAs) for IR imaging camera applications.

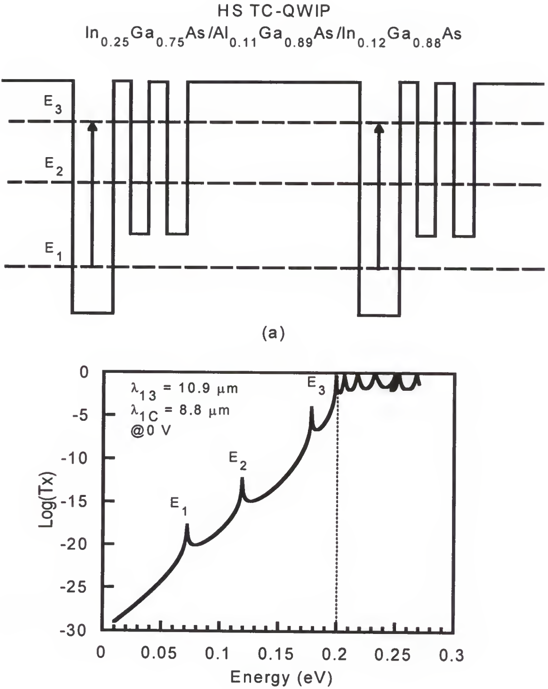

(a)

(b)

Figure 7.1. (a) The schematic conduction band diagram and (b) the transmission coefficient of the high strain TC-QWIP for LWIR detection.

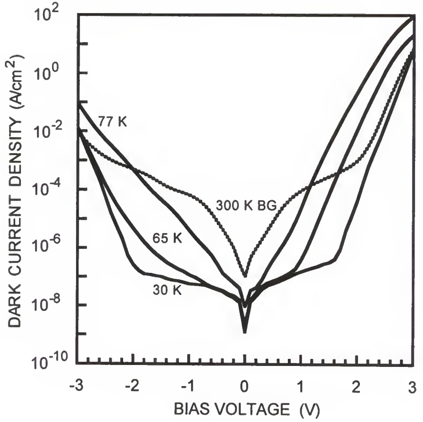

Figure 7.2. The dark *J-V* curves for the 5-period HS TC-QWIP.

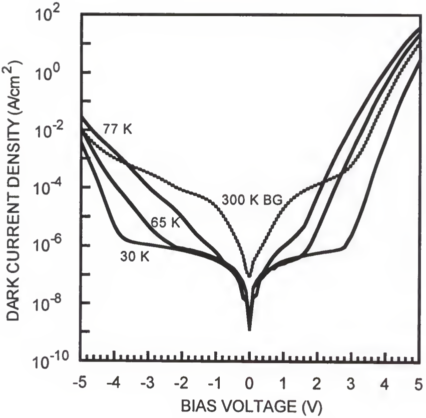

Figure 7.3 The dark *J-V* curves for the 10-period HS TC-QWIP.

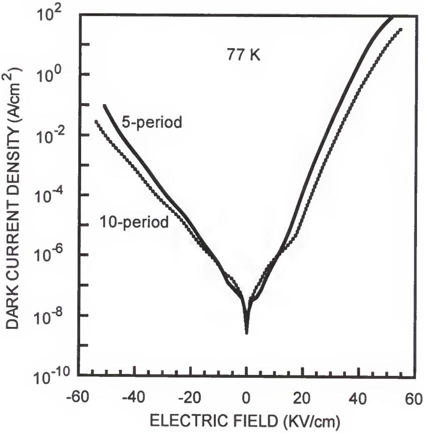

Figure 7.4. The dark current density versus electric field at 77 K for both 5-period and 10-period HS TC-QWIPs.

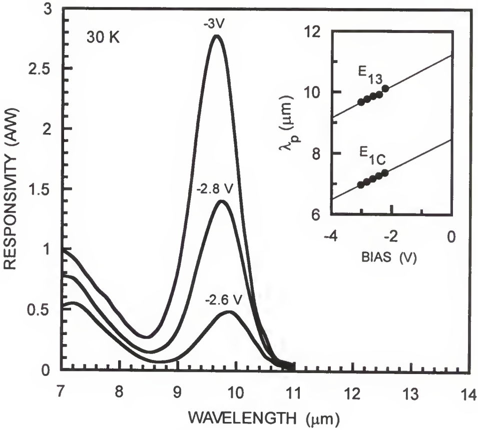

Figure 7.5. The spectral responsivities for the 5-period HS TC-QWIP with a 45° incidence measured at 30 K.

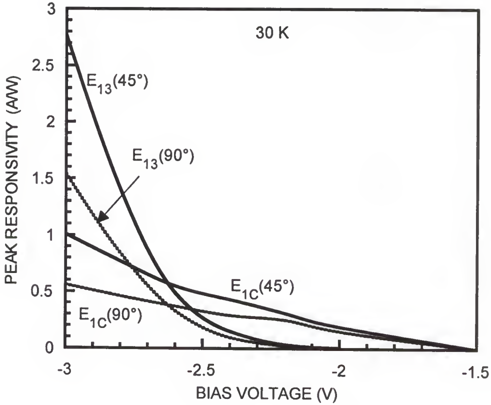

Figure 7.6. The peak responsivities versus bias for the 5-period HS TC-QWIP with 45° incidence and normal incidence measured at 30 K.

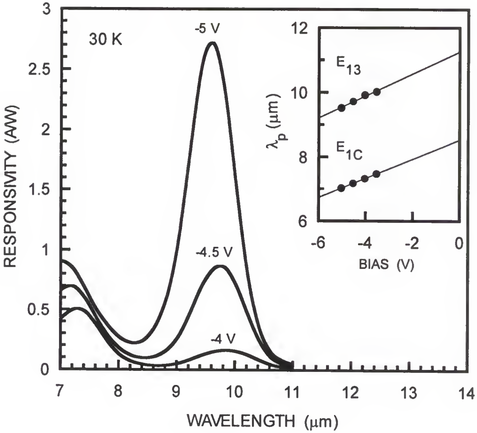

Figure 7.7. The spectral responsivities for the 10-period HS TC-QWIP with a 45° incidence measured at 30 K.

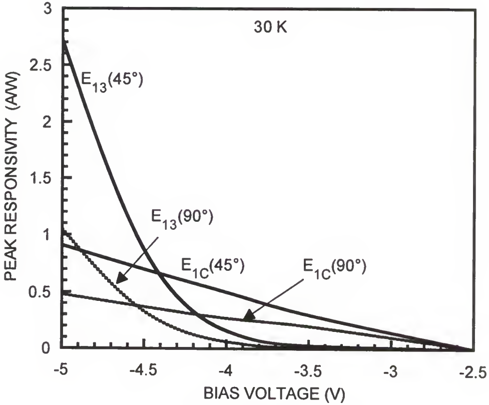

Figure 7.8. The peak responsivities versus bias for the 10-period HS TC-QWIP with 45° incidence and normal incidence measured at 30 K.

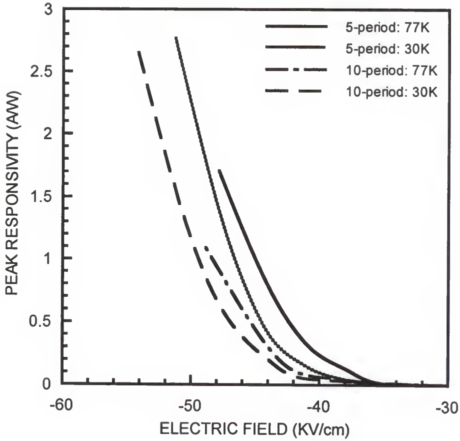

Figure 7.9. The temperature dependence of the peak responsivities for the $E_1 \rightarrow E_3$ transition versus electric field with a 45° incidence.

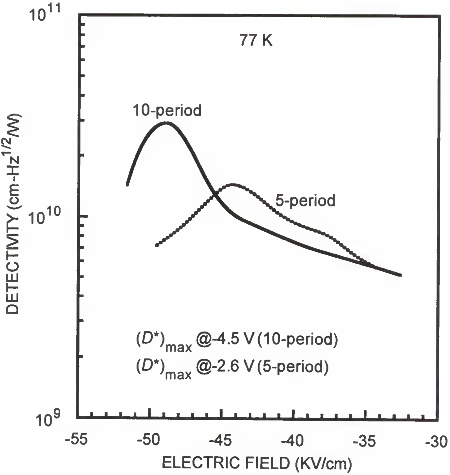

Figure 7.10. Detectivity versus electric field for the high strain TC-QWIP at 77 K.

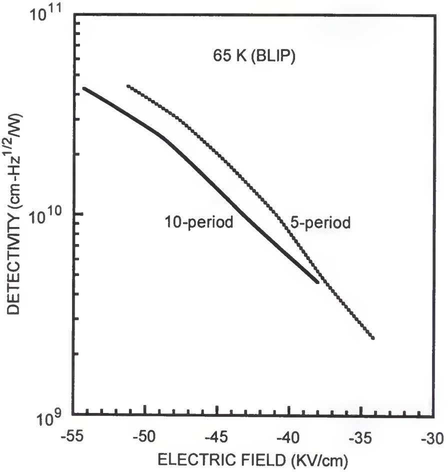

Figure 7.11. BLIP detectivity versus electric field for the high strain TC-QWIP at 65 K.

CHAPTER 8
SUMMARY AND CONCLUSIONS

In this dissertation, we investigate three new types of multicolor *n*-type quantum well infrared photodetectors (QWIPs) for 3 – 5 μm mid-wavelength infrared (MWIR) and 8 – 14 μm long-wavelength infrared (LWIR) dual-band detection. These are (1) a MWIR GaAs/AlAs/AlGaAs and a LWIR GaAs/AlGaAs stacked QWIP, (2) a two-stack two-color high strain InGaAs/GaAs/AlGaAs MWIR and a GaAs/AlGaAs LWIR QWIP, and (3) a two-stack indirect-barrier/triple-coupled (IB/TC) QWIP. In addition, three voltage-tunable multicolor *n*-type InGaAs/GaAs/AlGaAs triple-coupled (TC-) QWIPs with different indium compositions and doping densities in the quantum well are developed for the 7 – 14 μm LWIR detection. These QWIP structures were grown by the molecular beam epitaxy (MBE) technique. Detectivity ranging from 10^9 to mid 10^{11} cm-Hz$^{1/2}$/W was obtained for these QWIPs at $T = 77$ K. We have also developed a very high performance voltage-tunable multicolor TC-QWIP for the LWIR detection using high-strain InGaAs/AlGaAs/InGaAs material systems, which has achieved a very high responsivity of 1.3 A/W and an estimated detectivity of 2.93×10^{10} cm-Hz$^{1/2}$/W at $\lambda_p = 9.6$ μm, $V_b = -4.5$ V, and $T = 77$ K under 45° facet illumination. This device also shows very large normal incidence absorption, leading to the possibility of fabricating large area gratingless HS TC-QWIP FPAs for IR imaging applications.

First, we demonstrated a new two-color two-stack MWIR GaAs/AlAs/AlGaAs BTQB QWIP and LWIR GaAs/AlGaAs BTM QWIP with photovoltaic (PV) and photoconductive (PC) dual-mode operation in the 3 – 5 μm and 8 – 14 μm atmospheric spectral windows. The PV mode detection scheme uses transition from the ground-state to the quasi-bound state of the MWIR-QWIP. The PC mode detection scheme has two different transitions, one is similar to the PV detection scheme and the other uses transition from the ground-state to the miniband of the LWIR-QWIP. The peak responsivity at zero bias (PV mode) was found to be 17 mA/W at $\lambda_p = 4.1$ μm, $T = 50$ K, with a $\Delta\lambda/\lambda_p = 15$ %. The peak responsivities for the PC mode detection, were found to be 25 mA/W at $\lambda_p = 4.1$ μm, $V_b = 1$ V, and $T = 50$ K, and 0.12 A/W at $\lambda_p = 11.6$ μm, $V_b = 3.2$ V, $T = 50$ K, with a bandwidth of $\Delta\lambda/\lambda_p = 18$ %. The PV responsivity was found to be 68 % of the PC responsivity at $\lambda_p = 4.1$ μm and $T = 50$ K, demonstrating the ability for an efficient PV mode operation at 3 – 5 μm MWIR band.

Next, we demonstrated a new voltage-tunable multicolor triple-coupled quantum well infrared photodetector (TC-QWIP) for LWIR detection. Two TC-QWIP structures, QWIP- A and B, with different quantum well and barrier parameters have been fabricated and analyzed. Using quantum confined Stark shift effect, the wavelength tunability by the applied bias voltage in the wavelength range of 8.2 – 9.1 μm and 10.8 – 11.5 μm for QWIP- A and B, respectively, have been demonstrated in this work. Multi-wavelength photoresponses have been observed in both QWIP- A and B under different bias voltages and polarity conditions. As predicted by the theoretical calculations, the ($E_1 \rightarrow E_3$) transition is the dominant process responsible for the observed large photoresponsivity in both devices.

Third, a high-strain two-stack, two-color QWIP has been demonstrated with very high performance. The device has 35 % of indium in the QW of the MWIR stack which produces high in-plane compressive strain. This strain enhances the responsivity of the MWIR stack while allowing the detection spectrum to cover the point of interest in the MWIR region. The detection peak wavelengths are at 4.3 μm and 9.6 μm and the corresponding maximum responsivities are 0.65 A/W and 0.55 A/W for the MWIR and LWIR stacks, respectively, with 45° light incidence. Normal incidence without grating coupling also achieved responsivity of 0.25 A/W for either one stack.

Fourth, characterizations of four two-stack IB/TC-QWIPs, with different doping densities ($N_d = 5\times10^{17}$ cm^{-3} and 1×10^{18} cm^{-3}) and different quantum well (QW) periods (20 and 40 periods) have been performed to study the effects of doping density and QW period on the performance of these devices. The responsivity of the MWIR IB-QWIPs was found to increase with increasing doping density, while for LWIR TC-QWIPs the responsivity was found to vary very little with the doping density. Study of the effect of QW period reveals that the responsivity of the 20-period stacked-QWIP is better than that of the 40-period stacked-QWIP. The two-stack IB/TC-QWIPs reported here maybe used to detect simultaneously two colors in the MWIR and LWIR bands at the same bias voltage. It can also be used as a voltage tunable (PV and PC mode operation) two- or three-color QWIP for MWIR and LWIR dual band detection.

Fifth, we demonstrated a very high performance TC-QWIP using high strain *n*-type $In_{0.25}Ga_{0.75}As/Al_{0.11}Ga_{0.89}As/In_{0.12}Ga_{0.88}As$ asymmetrical coupled quantum well structure for 8 – 14 μm LWIR detection. The maximum responsivities at $\lambda_p = 9.6$ μm were found to be 1.71 A/W and 2.77 A/W at $V_b = -2.8$ V, -3 V and $T = 77$ K, 30 K, respectively, for the 5-period device. For the 10-period device, the maximum responsivities were found to be 1.3 A/W and 2.71 A/W at $\lambda_p = 9.7$ μm, $V_b = -4.5$ V, and $T = 77$ K, and at $\lambda_p = 9.6$ μm, $V_b = -5$ V, and $T = 30$ K, respectively. The maximum detectivities were found to be 1.44×10^{10} cm-Hz^{½}/W and 2.93×10^{10} cm-Hz^{½}/W at $\lambda_p = 9.8$ μm, $V_b = -2.6$ V and $T = 77$ K, and at $\lambda_p = 9.8$ μm, $V_b = -4.5$ V, and $T = 77$ K for the 5-period and 10-period devices, respectively. It is shown that this HS TC-QWIP can be used as a voltage-tunable two-color or multicolor QWIP for lower background LWIR detection. Furthermore, due to the very high responsivity and large normal incidence absorption observed in this device, it is possible to fabricate large area FPAs without using the grating coupler in this HS TC-QWIP.

Table 8.1 compares the device performance of the *n*-type QWIPs developed in this work and those published in the literature by other researchers. The results show that

QWIP-7 (HS TC-QWIP, described in chapter 7) has the highest responsivity with 45° incidence and $T = 77$ K. Figure 8.1 shows the detectivity versus cutoff wavelength for the *n*-type QWIPs which are studied in this dissertation and those published in the literature. The straight line is the result calculated from an empirical formula, which is given by [12]

$$D_c^* = 1.1 \times 10^6 e^{E_c/(2kT)} \ \mathrm{cm}\sqrt{\mathrm{Hz}}\,/\,\mathrm{W},$$

where E_c is cutoff energy and $T = 77$ K is the operating temperature. The results also show that the HS TC-QWIP has an outstanding performance at the cutoff wavelength of 10.2 μm.

There are several works need to be surveyed. Due to the high performance and the wavelength tunability of the HS TC-QWIP for the LWIR detection, it is recommended to design a similar structure for the MWIR detection and a broadband HS TC-QWIP using stacked structure for the 8 – 14 μm LWIR detection. In addition, a theoretical model of the HS TC-QWIP should be explored to optimize the device. We have also shown that high performance gratingless MWIR and LWIR QWIPs can be achieved using the high-strain InGaAs/AlGaAs material systems grown on the GaAs substrate. Several theoretical models have been proposed to explain this phenomenon, but none of these theories can quantitatively explain the experimental data. Therefore, a theoretical exploring on the normal incident absorption should be surveyed. The goal of this study is to achieve an optimized gratingless two-stack QWIP for the 3 – 5 μm MWIR and 8 – 14 μm LWIR dual-band detection.

Table 8.1. A comparison of the device performance of *n*-type LWIR QWIPs developed in this work and those published in the literature.

QWIP	Bias (V)	T (K)	λ_p (μm)	coupling method	R_i (A/W)	D^* (cm-Hz$^{1/2}$/W)
1	-3	70	8.5	45°	0.3	2×10^{11}
2	1.25	77	8.8	90°	0.23	1×10^{10}
3	-2	60	9.1	2D-grating	0.36	8×10^{10}
4	7	60	9.3	45°	0.19	1×10^{10}
5	2	70	9.4	45°	0.55	1.8×10^{10} (BLIP)
				90°	0.2	1.1×10^{10} (BLIP)
6	-4	60	9.6	45°	0.03	1×10^{10} (BLIP)
7	-4.5	77	9.8	45°	1.3	2.9×10^{10}
8	2.5	77	9.8	45°	0.6	1.7×10^{10}
				90°	0.2	1×10^{10}
9	3	70	9.8	45°	1.2	2×10^{10}
10	-2	50	10.2	45°	0.26	1×10^{10} (BLIP)
11	4	40	11.2	45°	0.33	1.6×10^{10} (BLIP)

note: 1 - BTQB QWIP, Gunapala et al. [60].
2 - Normal incidence InGaAs/GaAs QWIP, Wang et al. [76].
3 - E-QWIP, Beck et al. [59].
4 - TC-QWIP C (Chapter 6).
5 - Two-stack two-color high strain QWIP (Chapter 5).
6 - 3-color QWIP, Tidrow et al. [62].
7 - HS TC-QWIP (Chapter 7).
8 - Normal incidence InGaAs/GaAs QWIP, Karunasiri et al. [37].
9 - BTC QWIP, Bethea et al. [58].
10 - BTC QWIP, Levine et al. [80].
11 - TC-QWIP B (Chapter 4).

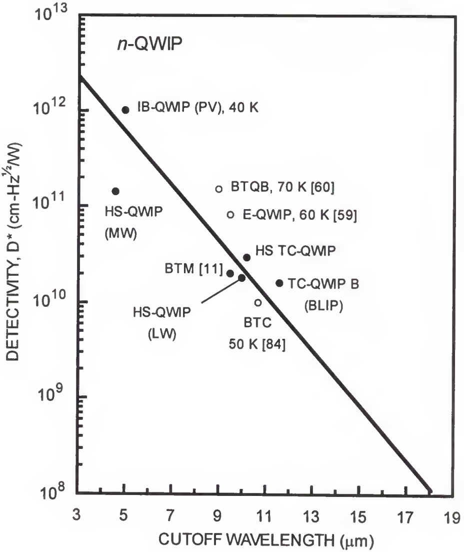

Figure 8.1. Detectivity versus cutoff wavelength for the *n*-type QWIPs developed in this work and those published in the literature.

APPENDIX 1
GLOSSARY OF SYMBOLS

α	absorption coefficient
δ_0	lattice-mismatch strain
Δf	noise spectral bandwidth
Δ_i	phase of the particle wave function in the specific layer
Δ_o	spin-orbit splitting energy
ΔE_a	activation energy
ΔE_C	bandoffset of the conduction band
ΔE_g	energy gap discontinuity
ΔE_H	hydrostatic component of the strain-induced energy shift
ΔE_U	shear uniaxial component of the strain-induced energy shift
ΔE_V	bandoffset of the valance band
ε	dielectric constant
ϕ_n	wave function of electron
Γ	full width at half maximum
η	quantum efficiency
λ_c	cutoff wavelength
λ_p	peak wavelength
μ_0	permeability in vacuum
μ_e	electron mobility

ν	frequency
σ	two-dimensional electron density
σ_c	cross-section area for electron trapping into the ground state
τ	lifetime
ω	angular frequency
a	lattice constant of the strained-layer
a_s	lattice constant of the substrate
A_d	area of detector
A_i	magnitude of the particle wave function in the specific layer
c	speed of light in vacuum
C_{ij}	elastic constants
D_p^*	non-BLIP peak detectivity
D_{BLIP}^*	BLIP detectivity
q	electron charge
E_b	barrier height
E_{co}	cutoff energy
E_F	Fermi energy
E_g	energy bandgap
E_n	energy level
E_{exch}	electron-electron exchange energy
F	electric field
f_{os}	dipole oscillator strength
g	optical gain
h	Plack's constant

$\hbar$	$h/(2\pi)$
I	current
I_A	integrated absorption strength
I_{BG}	intensity of the incident background
I_d	dark current
i_n	noise current
J	current density
J_d	dark current density
k	Boltzman's constant
k_w	wavevector in the well
k_b	wavevector in the barrier
k_z	wavevector in the growth direction
L_w	well width
L_b	barrier width
m^*	effective mass of electron
m_b^*	effective mass of electron in the barrier
M_{mn}	dipole matrix element
m_w^*	effective mass of electron in the well
N_C	effective density of states of the conduction band
N_d	doping density
N_{qw}	number of quantum well
Q_C	bandoffset ratio of the conduction band
Q_V	bandoffset ratio of the valence band
T	temperature

T_{BG}	background temperature
T_x	transmission coefficient
R_i	current responsivity
$R_{i,p}$	peak current responsivity
$V(z)$	conduction band potential energy in the growth direction
V_b	externally applied bias voltage
V_{cd}	conduction-band deformation potential
v_d	drift velocity
v_s	saturation drift velocity
V_{sd}	shear deformation potential
$W(\lambda)$	blackbody spectral density
z	z-axis, growth direction

APPENDIX 2
ACRONYMS

1-D	one-dimensional
2-D	two-dimensional
BLIP	background limited performance
BTB	bound-to-bound
BTC	bound-to-continuum
BTMB	bound-to-miniband
BTQB	bound-to-quasi-bound
CSL	compressively strained-layer
DB	double-barrier
DB-QWIP	double-barrier quantum well infrared photodetector
DBQW	double-barrier quantum well
FOV	field of view
FLIR	forward looking infrared
FPA	focal plane array
FWHM	full width at half maximum
HS	high-strain
HS TC-QWIP	high-strain triple-coupled quantum well infrared photodetector
I-V	dark current versus bias voltage
IB	indirect-barrier

IB-QWIP	indirect-barrier quantum well infrared photodetector
IR	infrared
J-V	dark current density versus bias voltage
LWIR	long-wavelength infrared
MBE	molecular beam epitaxy
MCT	HgCdTe
MOCVD	metalorganic chemical vapor depositon
MQW	multiple quantum well
MWIR	mid-wavelength infrared
PC	photoconductive
PV	photovoltaic
QCSE	quantum confined Stark effect
QW	quantum well
QWIP	quantum well infrared photodetector
TC	triple-coupled
TC-QWIP	triple-coupled quantum well infrared photodetector
TCQW	triple-coupled quantum well
TMM	transfer matrix method
TSL	tensile strained-layer
SI	semi-insulating

REFERENCES

1. R. B. Emmons, S. R. Hawkins, and K. F. Cuff, Opt. Eng. **14**, 21 (1975).
2. L. Esaki and T. Tsu, IBM J. Res. Develop. **14**, 61 (1970).
3. L. Serzhenko and V. D. Shadrin, Sov. Phys. Semicond. 25, 953 (1991).
4. L. L. Chang, L. Esaki, and G. A. Sai-Halaz, IBM Tech. Discl. Bull. **20**, 2019 (1977).
5. L. Esaki and H. Sakaki, IBM Tech. Discl. Bull. **20**, 2456 (1977).
6. D. D. Coon and R. P. G. Karunasiri, Appl. Phys. Lett. **45**, 649 (1984).
7. L. C. West and S. J. Eglash, Appl. Phys. Lett. **46**, 1156 (1985).
8. A. Harwit and J. S. Harris, Jr., Appl. Phys. Lett. **50**, 685 (1987).
9. B. F. Levine, K. K. Choi, C. G. Bethea, J. Walker, and R. J. Malik, Appl. Phys. Lett. **50**, 1092 (1987).
10. B. F. Levine, C. G. Bethea, G. Hasnain, V. O. Shen, E. Pelve, R. R. Abbot, and S. J. Hsieh, Appl. Phys. Lett. **56**, 851 (1990).
11. L. S. Yu and S. S. Li, Appl. Phys. Lett. **59**, 1332 (1991).
12. B. F. Levine, J. Appl. Phys. **74**, R1 (1993).
13. I. Gravé, A. Shakouri, N. Kuze, and A. Yariv, Appl. Phys. Lett. **60**, 2362 (1992).
14. A. Köck, E. Gornik, G. Abstreiter, G. Böhm, M. Walther, and G. Weimann, Appl. Phys. Lett. **60**, 2011 (1992).
15. K. K. Choi, B. F. Levine, C. G. Bethea, J. Walker, and R. J. Malik, Phys. Rev. **B 39**, 8029 (1989).
16. E. Martinet, E. Rosencher, F. Luc, P. Bois, E. Costard, and S. Delaitre, Appl. Phys. Lett. **61**, 246 (1992).

17. K. L. Tsai, K. H. Chang, C. P. Lee, K. F. Huang, J. S. Tsang, and H. R. Chen, Appl. Phys. Lett. **62**, 3504 (1993).

18. K. Kheng, M. Ramsteiner, H. Schneider, J. D. Ralston, F. Fuchs, and P. Koidl, Appl. Phys. Lett. **61**, 666 (1992).

19. A. Kastalsky, T. Duffield, S. J. Allen, and J. Harbison, Appl. Phys. Lett. **52**, 1320 (1988).

20. M. Z. Tidrow, K. K. Choi, C. Y. Lee, W. H. Chang, F. J. Towner, and H. R. Chen, Appl. Phys. Lett. **67**, 1800 (1995).

21. V. D. Shadrin and F. L. Serzhenko, Infrared Phys. **33**, 345 (1992).

22. M. A. Kinch and A. Yariv, Appl. Phys. Lett. **55**, 2093 (1989).

23. S. D. Gunapala, B. F. Levine, L. Pfeiffer, and K. West, J. Appl. Phys. **69**, 6517 (1991).

24. Z. Chen, S. Pan, S. Feng, D. Cui, and G. Yang, Infared Phys. **32**, 523 (1991).

25. G. Bastard, Phys. Rev. **B-24**, 5693 (1981).

26. D. Delagebeaudeuf, P. Deleckyse, P. Etienne, J. Massiers, M. Laviron, J. Chaplart, and T. Linh, Electron. Lett. **18**, 85 (1982).

27. I. Hase, H. Kawai, K. Kaneko, and K. Watanabe, Electron. Lett. **20**, 491 (1984).

28. P. J. Price, IBM J. Res. Develop. **17**, 39 (1973).

29. M. Artaki and K. Hess, Superlattice and Microstructures **1**, 489 (1985).

30. M. O. Manasreh, F. Szmulowicz, T. Vaughan, K. R. Evans, C. E. Stutz, and D. W. Fischer, Phys. Rev. **B 43**, 9996 (1991).

31. K. M. S. V. Bandara, D. D. Coon, and O. Byungsung, Phys. Lett. **53**, 1931 (1988).

32. J. -W. Choe, O. Byungsung, K. M. S. V. Bandara, and D.D. Coon, Appl. Phys. Lett. **56**, 1679 (1990).

33. Y. H. Wang, S. S. Li, J. Chu, and Pin Ho, Appl. Phys. Lett. **64**, 727 (1994).

34. Y. H. Wang, J. Chu, S. S. Li, and Pin Ho, J. Appl. Phys. **76**, 6009 (1994).

35. J. Chu, S. S. Li, and Pin Ho, Appl. Phys. Lett. **69**, 1258 (1986).

36. L. H. Peng, J. H. Smet, T. P. E. Broekaert, and C. G. Fonstad, Appl. Phys. Lett. **62**, 2413 (1993).

37. G. Karunasri, J. S. Park, J. Chen, R. Shih, J. F. Scheihing, and M. A. Dodd, Appl. Phys. Lett. **67**, 2600 (1995).

38. J. W. Mattews and A. E. Blackeslee, J. Crys. Growth **27**, 118 (1974).

39. G. E. Bir and G. E. Pikus, "Symmetry and Strain-Induced Effects in Semiconductors", J. Wiley, New York (1974).

40. S. H. Pan, H. Shen, Z. Hang, F. H. Pollak, W. Zhuang, Q. Xu, A. P. Roth, R. A. Masut, C. Lacelle, and D. Morris, Phys. Rev. **B-38**, 3375 (1988).

41. B. F. Levine, R. J. Malik, J. Walker, K. K. Choi, C. G. Bethea, D. A. Kleinman, and J. M. Vandenberg, Appl. Phys. Lett. **50**, 273 (1987).

42. G. D. Sanders and Y. C. Chang, Phys. Rev. **35**, 1300 (1987).

43. E. J. Roan and S. L. Chuang, J. Appl. Phys. **69**, 3249 (1991).

44. D. L. Smith and C. Mailhiot, Rev. Mod. Phys. **62**, 173 (1990).

45. S. Mori and T. Ando, Surf. Sci. **98**, 101 (1980).

46. D. Ahn and S.-L. Chuang, IEEE J. Quantum Electron. **QE-23**, 2196 (1987).

47. G. Hasnain, B. F. Levine, C. G. Bethea, R. A. Logan, J. Walker, and J. Malik, Appl. Phys. Lett. **54**, 2515 (1989).

48. Y. C. Wang and S. S. Li, J. Appl. Phys. **75**, 582 (1994).

49. H. Schneider, E. C. Larkins, J. D. Ralston, K. Schwarz, F. Fuchs, and P. Koidl, Appl. Phys. Lett. **63**, 782 (1993).

50. B. F. Levine, C. G. Bethea, G. Hasnain, J. Walker, and R. J. Malik, Appl. Phys. Lett. **53**, 296 (1988).

51. D. C. Wang, Ph.D. Dissert., Univ. of Florida (1996).

52. A. Zussman, B. F. Levine, J. M. Kuo, and J. de Jong, J. Appl. Phys. **70**, 5101 (1991).

53. J. S. Smith, L. C. Chiu, S. Margalit, A. Yariv, and A. Y. Cho, J. Vac. Sci. Technol. **B 1**, 376 (1983).

54. L. S. Yu, Y. H. Wang, and S. S. Li, Appl. Phys. Lett. **60**, 992 (1992).

55. C. G. Bethea, B. F. Levine, M. T. Asom, R. E. Leibengnth, J. W. Stayt, K. G. Glogovsky, R. A. Morgan, J. D. Blackwell, and W. J. Parrish, IEEE Trans. Electron Devices **ED-40**, 1957 (1993).

56. Y. H. Wang, S. S. Li, and P. Ho, Appl. Phys. Lett. **62**, 93 (1993).

57. Y. H. Wang, S. S. Li, and P. Ho, Appl. Phys. Lett. **62**, 621 (1993).

58. C. G. Bethea, B. F. Levine, V. O. Shen, R. R. Abbot, and S. J. Hsieh, IEEE Trans. Electron Devices **ED-38**, 1118 (1991).

59. W. A. Beck, T. S. Faska, J. W. Little, A. C. Goldberg, J. Albritton, and M. Sensiper, in Proceedings of the 3rd International Symposium on Long Wavelength Infrared Detectors and Arrays **ECS-95-28**, 7 (1995)

60. S. D. Gunapala, J. K. Liu, M. Sundaram, J. K. Park, C. A. Shott, T. I. Lin, S. T. Massie, P. D. Marker, R. E. Muller, and G. Sarusi, in Proceedings of the 3rd International Symposium on Long Wavelength Infrared Detectors and Arrays **ECS-95-28**, 55 (1995)

61. H. C. Liu, J. Li, J. R. Thompson, Z. R. Wasilewski, M. Buchanan, and J. G. Simmons, IEEE Electron Device Lett. **EDL-14**, 556 (1993).

62. M. Z. Tidrow, K. K. Choi, C. Y. Lee, W. H. Chang, F. J. Towner, and H. R. Chen, Appl. Phys. Lett. **64**, 1268 (1994).

63. Y. H. Wang, J. C. Chiang, S. S. Li, and P. Ho, J. Appl. Phys. **76**, 2538 (1994).

64. C. J. Chen, K. K. Choi, M. Z. Tidrow, and D. C. Tsui, Appl. Phys. Lett. **68**, 1446 (1996).

65. Y. Huang and C. Lien, J. Appl. Phys. **77**, 3433 (1995).

66. D. C. Wang, G. Bosman, and S. S. Li, J. Appl. Phys. **79**, 1486 (1996).

67. A. Foire, E. Rosencher, P. Bois, J. Nagle, and N. Laurent, Appl. Phys. Lett. **64**, 478 (1994).

68. L. H. Peng and C. G. Fonstad, J. Appl. Phys. **77**, 747 (1995).

69. J. C. Chiang, S. S. Li, M. Z. Tidrow, P. Ho, C. M. Tsai, and C. P. Lee, Appl. Phys. Lett. **69**, 2412 (1996).

70. B. F. Levine, A. Y. Cho, J. Walker, R. J. Malik, D. A. Kleinman, and D. L. Sivco, Appl. Phys. Lett. **52**, 1481 (1988).

71. L. S. Yu, S. S. Li, and Pin Ho, Appl. Phys. Lett. **59**, 2712 (1991).

72. R. P. G. Karunasiri, J. S. Park, and K. L. Wang, Appl. Phys. Lett. **59**, 2588 (1991).

73. J. S. Park, R. P. G. Karunasiri, and K. L. Wang, Appl. Phys. Lett. **59**, 2588 (1991).

74. T. L. Lin and J. Maserjian, Appl. Phys. Lett. **57**, 1142 (1990).

75. B. F. Levine, S. D. Gunapala, and R. F. Kopf, Appl. Phys. Lett. **58**, 1551 (1991).

76. S. Y. Wang and C. P. Lee, Appl. Phys. Lett. **71**, 119 (1997).

77. J. Y. Andersson, L. Lundqvist, and Z. F. Paska, Appl. Phys. Lett. **58**, 2264 (1991).

78. S. D. Gunapala, K. M. S. V. Bandara, B. F. Levine, G. Sarusi, D. L. Sivco, and A. Y. Cho, Appl. Phys. Lett. **64**, 2288 (1994).

79. S. D. Gunapala, K. M. S. V. Bandara, B. F. Levine, G. Sarusi, J. S. Park, T. L. Lin, W. T. Pike, and J. K. Liu, Appl. Phys. Lett. **64**, 3431 (1994).

80. B. F. Levine, G. Hasnain, C. G. Bethea, and N. Chand, Appl. Phys. Lett. **54**, 2704 (1989).

BIOGRAPHICAL SKETCH

Jung-Chi Chiang was born in Taiwan, Republic of China on April 6, 1959. He received a Bachelor of Science degree from the Department of Electrophysics of National Chiao Tung University in June, 1981. In June, 1983, he received a Master of Science degree from the Institute of Electro-Optics of National Chiao Tung University. After graduation, he worked in Chung San Institute of Science and Technology, Lungtan, Taiwan, Republic of China as a research scientist from 1983 to 1991. During this period, he received the President's outstanding research award in December, 1988.

In August of 1991, he enrolled in the Department of Electrical and Computer Engineering of the University of Florida, and began his Ph.D. research on the development of multicolor quantum well infrared photodetectors for the mid- and long-wavelength infrared imaging array applications.

I certify that I have read this study and that in my opinion it conforms to acceptable standards of scholarly presentation and is fully adequate, in scope and quality, as a dissertation for the degree of Doctor of Philosophy.

Sheng San Li

Sheng S. Li, Chair
Professor of Electrical and Computer Engineering

I certify that I have read this study and that in my opinion it conforms to acceptable standards of scholarly presentation and is fully adequate, in scope and quality, as a dissertation for the degree of Doctor of Philosophy.

Gijs Bosman
Professor of Electrical and Computer Engineering

I certify that I have read this study and that in my opinion it conforms to acceptable standards of scholarly presentation and is fully adequate, in scope and quality, as a dissertation for the degree of Doctor of Philosophy.

Arnost Neugroschel

Arnost Neugroschel
Professor of Electrical and Computer Engineering

I certify that I have read this study and that in my opinion it conforms to acceptable standards of scholarly presentation and is fully adequate, in scope and quality, as a dissertation for the degree of Doctor of Philosophy.

Robert M. Park

Robert M. Park
Professor of Material Science and Engineering

I certify that I have read this study and that in my opinion it conforms to acceptable standards of scholarly presentation and is fully adequate, in scope and quality, as a dissertation for the degree of Doctor of Philosophy.

Meimei Z. Tidrow
Courtesy Associate Professor of Electrical and Computer Engineering

This dissertation was submitted to the Graduate Faculty of the College of Engineering and to the Graduate School and was accepted as partial fulfillment of the requirements for the degree of Doctor of Philosophy.

December 1997

Winfred M. Phillips
Dean, College of Engineering

Karen A. Holbrook
Dean, Graduate School